J. Fluid Mech. (2023), *vol*. 975, A19, doi:10.1017/jfm.2023.818

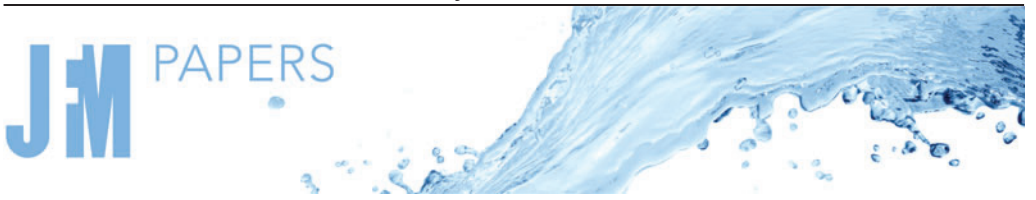

Turbulent boundary layer flow over a three-dimensional sinusoidal surface

C.I. Chan[1,2] **and R.C. Chin**[1,†]

[1]School of Electrical and Mechanical Engineering, University of Adelaide, South Australia 5005, Australia

[2]Graduate School of Engineering Science, Osaka University, 1-3 Machikaneyama, Toyonaka, Osaka 560-8531, Japan

(Received 12 February 2023; revised 17 September 2023; accepted 28 September 2023)

The sinusoidal roughness effect is investigated using a direct numerical simulation (DNS) of a spatially developing turbulent boundary layer (TBL) over three-dimensional sinusoidal roughness. The validity of Townsend's outer-layer similarity hypothesis is assessed based on comparisons of mean and second-order flow statistics, with a DNS of smooth-wall TBL data set at a similar Reynolds number. The total, Reynolds and dispersive stress tensors are calculated using the double-averaging procedure. The mean and second-order statistical similarities in the outer layer between rough-wall and smooth-wall TBLs are generally observed. The transport between total, turbulent and dispersive kinetic energy is investigated utilising triple-decomposed kinetic energy transports equations. The transport behaviour of turbulent kinetic energy (TKE) is significantly affected by the local mean shear induced by the surface roughness. However, the TKE transport shows good collapse with the smooth-wall case in the outer region of the flow. On the other hand, the transport of dispersive kinetic energy, including local production, redistribution and dissipation, are confined within the roughness sublayer. The intercomponent transfer between TKE and dispersive kinetic energy is quantified from the triple-decomposed kinetic energy transport equations. The intercomponent energy transfer is associated with the local spatial gradients of the turbulent momentum fluxes generated near the roughness canopy.

Key words: turbulent boundary layers, turbulence simulation

1. Introduction

Turbulent flow over rough walls has long been a subject of research as the rough walls influence the flow characteristics, such as heat and momentum transports. While turbulent

† Email address for correspondence: rey.chin@adelaide.edu.au

flows over smooth walls are well understood, the characteristics of turbulent flows over rough walls are less predictable than those of smooth walls because the flows are subjected to properties of the roughness (Raupach, Antonia & Rajagopalan 1991; Krogstad & Antonia 1994; Jiménez 2004; Kadivar, Tormey & McGranaghan 2021), such as the roughness packing density (i.e. closely packed or sparsely packed), roughness geometry (i.e. regular roughness such as sinusoidal, cubical and spherical or irregular/random roughness), in-plane wavelengths (i.e. varying two-dimensional or three-dimensional roughness heights) and flow types between different geometries such as pipe, closed channel and boundary layer flows. Thus, developing a universal model to predict, e.g. frictional drag on rough walls, remains challenging (Flack & Schultz 2010, 2014; Chung *et al.* 2021).

One of the longstanding interests in studying rough-wall-bounded turbulent flows is to assess the validity of Townsend's wall similarity hypothesis (Townsend 1956). The wall similarity hypothesis conjectured that the turbulence above the roughness sublayer extending to the outer region is independent of the wall surface conditions at sufficiently high Reynolds numbers. The statement equivalently states that both the turbulence intensity and the velocity defect profiles scale with friction velocity, independent of roughness and Reynolds number in the outer region, namely the outer-layer similarity (Raupach *et al.* 1991; Jiménez 2004; Flack & Schultz 2014; Chung *et al.* 2021), among others. Turbulent boundary layer (TBL) flows over regular/irregular and two/three-dimensional roughnesses were studied experimentally and numerically to explore how different types of roughness elements impact on the mean flow and turbulence quantities (e.g. Krogstad, Antonia & Browne (1992), Krogstad & Antonia (1994), Flack, Schultz & Shapiro (2005), Krogstad *et al.* (2005), Lee & Sung (2007), Volino, Schultz & Flack (2011), Flack & Schultz (2014), Medjnoun *et al.* (2021), Abdelaziz *et al.* (2022), among others. Rough-wall TBL studies by Krogstad *et al.* (1992) suggested that the mean velocity and turbulence intensity profiles were affected by the roughness well into the outer region of the TBL, as well as showing an increased fourth quadrant activity of the Reynolds shear stress near the roughness surface. It was concluded that the roughness effects were not confined to the near-wall region (Krogstad & Antonia 1994). Krogstad *et al.* (2005) studied rod-roughened turbulent channel flows and showed that no influence of surface roughness in the outer region was observed in the first-order mean flow statistics, but evidence of outer flow dissimilarity was observed from the second-order statistics and in terms of the turbulence structures.

Recent studies on rough-wall flows have yielded different conclusions because the outer-layer similarity depends on a great variety of factors, such as the roughness topology, type of flow and roughness length scales (for a comprehensive discussion, see the recent review (Chung *et al.* 2021)). There are fundamental differences between TBL flows over two-dimensional roughness and three-dimensional roughness, e.g. Flack *et al.* (2005), Schultz & Flack (2005), Volino, Schultz & Flack (2009), Wu & Christensen (2010), Volino *et al.* (2011), Lee, Sung & Krogstad (2011), Krogstad & Efros (2012*a*), Flack & Schultz (2014), Yang *et al.* (2016), among others. Volino *et al.* (2009) studied the outer-layer structure of a TBL over two-dimensional roughness and found that the two-dimensional roughness enhanced the flow motions associated with the roughness length scale, resulting in outer-layer modifications of the Reynolds stresses. Lee & Sung (2007) performed direct numerical simulation (DNS) studies of TBL over two-dimensional surface roughness and reported dissimilarities of the Reynolds stresses in the outer region between rough-wall and smooth-wall flows. Subsequently, Lee *et al.* (2011) conducted DNS of a TBL over a cube-roughened wall with three-dimensional disturbances. They found that two-dimensional and three-dimensional surface elements affect the Reynolds stress

distributions in the outer layer. Flack *et al.* (2005) and Schultz & Flack (2005) studied the TBLs over three-dimensional regular and irregular rough surfaces and found that the first-, second- and higher-order turbulent statistics outside the roughness sublayer were independent of the wall conditions. The wall independence was confirmed by quadrant analysis of the Reynolds shear stress, which indicated that the differences in the rough-wall boundary layers were confined to the near-wall region (with distance of the order of the equivalent sand roughness height). There is a suggestion that sufficient scale separation is necessary between the roughness length scale and the outer length scale of the flow, i.e. the boundary layer thickness is large compared with the equivalent sand roughness height $\delta/k_s \geq 40$ or equivalently, between boundary layer thickness and roughness height δ/k (Jiménez 2004). However, it has been shown that the criterion using sand roughness height depends on the roughness type and is not universally applicable. The outer-layer similarity may not solely depend on δ/k_s or δ/k but also depends on the roughness morphology (Placidi & Ganapathisubramani 2018; Womack *et al.* 2022). Volino *et al.* (2011) studied two-dimensional bars and three-dimensional cubes in TBLs. The authors found that two-dimensional bars with a much smaller roughness height, or k_s/δ, cause a much more significant effect on turbulent structures than the three-dimensional cubes in the outer part of the boundary layer. Yang *et al.* (2016) showed that two-dimensional roughness generally has relatively stronger sheltering effects than three-dimensional roughness, due to a smaller roughness height-to-width ratio. Krogstad & Efros (2012*a*) suggested that for transverse bar roughness, relatively high δ/k and Reynolds number are required for outer-layer similarity to hold.

It is still a question whether or not TBLs over three-dimensional sinusoidal roughness will follow a similar trend to the previous pipes and channels studies, in which evidence of the outer-layer similarity in internal flows for certain k_s^+ thresholds was observed (Chan *et al.* 2015; Ma *et al.* 2020). For example, there have been studies showing that TBL over cube roughness, in which the wall-similarity could not be observed, which was viewed as the fundamental difference between external and internal flows (TBL, pipe and channel flows) (Lee *et al.* 2011). The diagnostic plot reveals a linear asymptote between the mean flow and turbulent fluctuation, in the region extending from the logarithmic region to the outer wake region of zero-pressure-gradient (ZPG) TBLs (Alfredsson, Segalini & Örlü 2011; Castro, Segalini & Alfredsson 2013), independent of whether the surface condition is smooth or fully rough. However, it can be observed that the universal scaling does not seem to apply across different flow types, such as when comparing the results of rough-wall ZPG TBLs with the channel studies (Forooghi *et al.* 2018; Stroh *et al.* 2020). In addition, it is worth noting that some of the observed roughness effects exhibit dependencies on Reynolds numbers. The roughness effects may undergo significant changes with increased friction Reynolds number and k^+, leading to an increasing roughness function (Busse, Thakkar & Sandham 2017).

Nevertheless, there is much literature on numerical studies of turbulent pipe and channel flows over three-dimensional regular closely packed roughness, e.g. DNS of cube arrays in channel flows (Leonardi & Castro 2010; Xu *et al.* 2021), DNS of open channel flows over spherical shaped elements (Chan-Braun, García-Villalba & Uhlmann 2011), three-dimensional sinusoidal roughness in DNS of pipe flows (Chan *et al.* 2015) and in DNS of channel flows (Macdonald *et al.* 2016; Ma *et al.* 2020). Also, the examples of simulations of TBLs with three-dimensional regular roughness most commonly found in the literature are studies of cubical roughness in TBLs (e.g. Lee *et al.* 2011, 2012; Nadeem *et al.* 2015; Blackman & Perret 2016; Yang *et al.* 2016; Hwang & Lee 2018; Yang *et al.* 2019). In comparison, there have been relatively limited investigations of spatially developing TBLs over three-dimensional sinusoidal roughnesses. One of the aims of the

present study is to investigate the three-dimensional sinusoidal rough wall in TBLs at a higher Reynolds number range than previous studies to examine the outer-layer similarity and provide a new data set for TBLs with three-dimensional sinusoidal roughnesses.

The range of Reynolds numbers considered in the present study is determined by the simulation of spatially developing TBL that require a sufficiently long streamwise domain extent for the smooth-wall inflow to develop a fully rough-wall flow state. The present study also attempts to provide an in-depth analysis of Reynolds stress and dispersive stress transports. The Reynolds stress and dispersive stress transports arise because of the strong spatial inhomogeneities with rough-wall flows. This paper attempts to gain better insight into the development of two types of kinetic energy transports during TKE and dispersive kinetic energy generation and provides a relatively more straightforward but valuable model for studying kinetic energy balance in rough-wall flows.

Although the Reynolds and dispersive stresses for regular and irregular roughness surfaces were intensively studied by, for example, Poggi, Katul & Albertson (2004), Coceal *et al.* (2006), Coceal, Thomas & Belcher (2007*b*), Bailey & Smits (2010), Anderson *et al.* (2015), Vanderwel *et al.* (2019), Ma, Alamé & Mahesh (2021), Womack *et al.* (2022) and many others, there remains a need for more in-depth analysis and a demand for simple and convenient methods to investigate the distributions of Reynolds and dispersive stresses. Recently, Vanderwel *et al.* (2019) studied a TBL over ridge-type roughness and found that the dispersive stress was not only present in the vicinity of the surface roughness but also strongly augments the Reynolds stress in the outer region: $y/\delta > 0.1$. Vanderwel *et al.* (2019) demonstrated that the formation of the large-scale secondary motions may play an essential role in the outer-layer distribution of the dispersive stress for both regular and irregular roughness flows. On the other hand, Ma *et al.* (2021) conducted DNS of turbulent channel flow over random rough surfaces and found that the dispersive stresses are mostly confined to the roughness sublayer. The distribution of the dispersive stress varies with different types of roughness and flow geometry. Different types and arrangements of roughness exhibit distinct characteristics of the secondary flow, which in turn influence the distribution of dispersive stress (Stroh *et al.* 2020; Womack *et al.* 2022). The Reynolds and dispersive energy transport equations are valuable tools for the detailed analysis of the energy processes associated with turbulent and dispersive stress distribution. The second aim of this study is to present an analysis of these energy components, exploring their transport mechanisms and respective contributions to the overall energy distribution.

2. Methodology

2.1. *Numerical method*

An incompressible ZPG TBL over a three-dimensional sinusoidal rough wall has been considered. The streamwise, wall-normal and spanwise coordinates are denoted interchangeably as $\boldsymbol{x} = (x, y, z)$ or x_i $(i = 1, 2, 3)$. The corresponding instantaneous velocity components are denoted interchangeably as $\boldsymbol{u} = (u, v, w)$ or u_i. Time-averaged quantities are denoted by an overbar $(\bar{\cdot})$ and their fluctuation based on the Reynolds decomposition is denoted by a prime $(')$. The superscript $+$ refers to scaling with the friction velocity $u_\tau = \sqrt{\tau_w/\rho}$ and kinematic viscosity ν, where τ_w is the mean wall shear stress and ρ is the constant fluid density. The incompressible Navier–Stokes equations are solved using the spectral solver SIMSON (Chevalier, Lundbladh & Henningson 2007). The computational domains in the streamwise, wall-normal and spanwise directions are, respectively, $L_x \times L_y \times L_z = 8000\delta_0^* \times 200\delta_0^* \times 240\delta_0^*$ using $8192 \times 641 \times 768$ spectral modes, where δ_0^* is the displacement thickness at the inlet of the domain.

Spatial discretisation is based on a Fourier series with 3/2 zero-padding for dealiasing in the streamwise and spanwise directions, and the number of grid points in the streamwise and spanwise direction is therefore increased by a factor of 3/2 due to the dealiasing. A Chebyshev polynomial is employed in the wall-normal direction. To impose a streamwise periodic boundary condition, a fringe region is employed close to the end of the computational domain. The flow is damped via a volume force in the fringe region until it returns to the inflow condition (Schlatter & Örlü 2010). A low-amplitude volume force trip is applied to the Navier–Stokes equations at the region close to the inlet to trigger a rapid transition to turbulent flow (Schlatter & Örlü 2012). The time advancement is carried out by a second-order Crank–Nicolson scheme for the viscous terms and a third-order four-stage Runge–Kutta scheme for the nonlinear terms (Chevalier *et al.* 2007).

2.2. *Roughness implementation and description*

In this study, the rough wall is a three-dimensional surface defined as

$$h_k(x, z) = h_0 + h_0 \cos\left(\frac{2\pi x}{\Omega_x}\right) \cos\left(\frac{2\pi z}{\Omega_z}\right). \tag{2.1}$$

Figure 1 shows a schematic diagram of the rough wall. Here, Ω_x and Ω_z are the streamwise and spanwise roughness wavelengths, which are fixed constants. We let $\Omega_x = \Omega_z = \Omega$ so that the roughness is regular. Here h_0 is the roughness half-height, i.e. half of the peak to trough roughness height. From (2.1), we define the roughness height as the semiamplitude, i.e. $k = h_0$. The rough wall is modelled by the immersed boundary method (IBM). The IBM constitutes an extra forcing term introduced to the Navier–Stokes equation, where no-slip and non-penetration boundary conditions are obtained on the rough wall by enforcing zero velocities at the nearest grid points. The same numerical scheme has been successfully implemented in previous studies (Chan & Chin 2022; Chan *et al.* 2022). Regarding the grid resolution for the surface roughness, first, in the present simulation, all the cases are expected to be in the fully rough regime. The wall-normal grid resolution near the rough-wall region was determined such that the grid spacing is less than $\Delta y^+_{rough,max} < 3$ in wall units. There are at least 54 Chebyshev collocation points within the region $y^+ < \max(h_k^+)$. Second, the ratios of the computational grid sizes to the roughness streamwise and spanwise wavelengths are, respectively, $\Delta x \simeq \Omega_x/30$ and $\Delta z \simeq \Omega_z/90$. The resolutions in the streamwise, wall-normal and spanwise directions are to ensure that the simulation is sufficient to capture the full range of length scales, including for both TBL and rough walls, as discussed by previous studies regarding grid resolution requirements for rough-wall simulations (Coceal *et al.* 2006; Busse, Lützner & Sandham 2015). As suggested by Busse *et al.* (2015) for most irregular rough surfaces, $\Omega_{min} > 12$ grid points per smallest wavelength of the surface give good resolutions of the surface topographies. It is expected that this can be applied to regular rough surfaces with a relatively larger and constant wavelength. The resolution of the present simulation is listed in table 1. Cases rDNS1, rDNS2 and rDNS3 are obtained from the same DNS and correspond to different Reynolds numbers. It is important to note that the sinusoidal roughness used in these cases is identical (i.e. with constant k/δ_0^*), see also table 2. The data set for the smooth-wall reference case, sDNS, is from Chan, Schlatter & Chin (2021). Regarding the grid resolution for the DNS of TBL, the Kolmogorov length scale $\eta \equiv (\nu^3/\epsilon)^{1/4}$ or $\eta^+ \equiv (\epsilon^+)^{-1/4}$ is computed based on the local average rate of energy dissipation per unit mass, i.e. $\epsilon = 2\nu\overline{\langle s_{ij}s_{ij}\rangle}$ where s_{ij} is the fluctuating rate of the strain tensor (Pope 2000). From table 3, the grid resolutions are

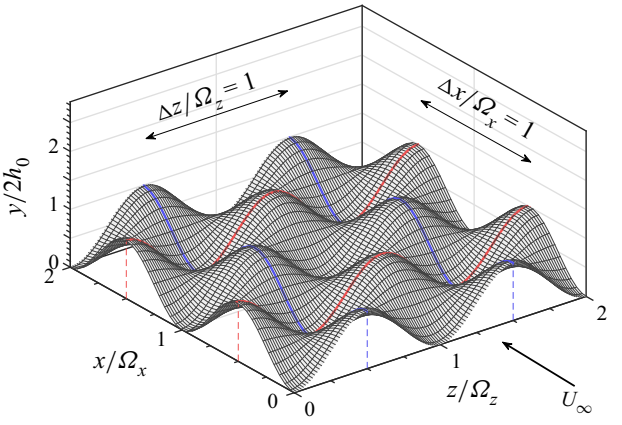

Figure 1. Schematic of the roughness geometry. Here, Ω_x and Ω_z are the streamwise and spanwise roughness wavelengths; h_0 is the roughness half-height (i.e. half of the peak to trough roughness height).

Case	$N_x \times N_y \times N_z$	$(L_x \times L_y \times L_z)/\delta_0^*$	Δx^+	$(\Delta y^+_{min}, \Delta y^+_{max})$	Δz^+
sDNS	$12\,800 \times 769 \times 1024$	$10\,000 \times 300 \times 360$	9	(0.02, 10)	4
rDNS1	$8192 \times 641 \times 768$	$8000 \times 200 \times 240$	15	(0.03, 11)	5
rDNS2	$8192 \times 641 \times 768$	$8000 \times 200 \times 240$	15	(0.03, 11)	5
rDNS3	$8192 \times 641 \times 768$	$8000 \times 200 \times 240$	15	(0.03, 11)	5

Table 1. Computation domain sizes and resolutions for smooth- and rough-wall cases. The reference smooth-wall case sDNS is from Chan *et al.* (2021). Here, N_x, N_y and N_z are the numbers of spectral collocation points in the streamwise, wall-normal and spanwise directions, respectively; L_x, L_y and L_z are the domain sizes scaled by δ_0^* in the streamwise, wall-normal and spanwise directions, respectively; δ_0^* is the displacement thickness at the inlet of the domain; Δx^+, Δy^+_{min}, Δy^+_{max} and Δz^+ are the corresponding grid resolutions in wall units.

of the order of η (i.e. $\Delta y^+ < 10\eta^+$). Also, the computational time step Δt^+ is shown to be much lower than the Kolmogorov time scale, which is defined as $t_\eta \equiv (\nu/\epsilon)^{1/2}$ or $t_\eta^+ \equiv (\epsilon^+)^{-1/2}$. Overall, the numerical set-up, including the domain size and grid resolution, are comparable with those employed in previous studies on rough-wall DNS of TBL (Lee *et al.* 2011; Cardillo *et al.* 2013; Nadeem *et al.* 2015). The computed Kolmogorov length and time scales in the present simulation suggest that the simulation is well resolved (Moin & Mahesh 1998; Choi & Moin 1994). Figure 2 shows the instantaneous streamwise velocity, mean streamwise velocity and mean streamwise vorticity contours, confirming that the rough-wall implementation is satisfactory. The present DNS was run for at least $\Delta T u_\tau^2/\nu \approx 14\,600$ before statistics were collected. Statistics were taken and averaged for at least $\Delta T u_\tau^2/\nu \approx 8800$.

Parameters that characterise the roughness surface are listed in table 2. The global averaged boundary layer parameters variations in the streamwise direction, including the (*a*) boundary layer thickness, (*b*) displacement thickness, (*c*) momentum thickness and (*d*) shape factor, are presented in figure 3. Compared with the smooth-wall TBL, the rough-wall TBL exhibits higher boundary layer parameters at the same streamwise distance. An important parameter to compare is the shape factor H, defined as the ratio of displacement to momentum thickness, characterising the development state

Case	Re_τ	Re_θ	h^+_{rms}	ES	h^+_a	k^+	k/δ	k/Ω	u_τ/U_∞	e^+
sDNS	2020	6650	—	—	—	—	—	—	0.0367	—
rDNS1	1780	4820	20.7	0.223	16.8	41.4	0.0233	0.0875	0.0526	23.7
rDNS2	2080	5880	19.8	0.223	16.0	39.5	0.0190	0.0875	0.0502	22.6
rDNS3	2820	7530	19.6	0.223	15.9	39.3	0.0139	0.0875	0.0499	22.5

Table 2. Reynolds numbers and rough-wall parameters of smooth-wall and rough-wall cases. Here $Re_\tau \equiv \delta^+$, where δ is the boundary layer thickness; $Re_\theta \equiv U_\infty\theta/\nu$, where θ is the momentum thickness; h^+_{rms} is the root-mean-square roughness height (2.2); ES is the effective slope (2.4); h_a is the mean roughness height (2.3); k^+ is the roughness height defined as the semiamplitude; Ω is the roughness wavelength; u_τ/U_∞ is the friction velocity; and e is the wall offset.

Case	y^+_e	$-\epsilon^+$	$(\Delta y^+, \eta^+)$	$(\Delta t^+, t^+_\eta)$	Case	y^+_e	$-\epsilon^+$	$(\Delta y^+, \eta^+)$	$(\Delta t^+, t^+_\eta)$
rDNS1	0.3	0.11	(1.68, 1.73)	(0.25, 2.98)	rDNS2	0.3	0.12	(1.60, 1.69)	(0.23, 2.85)
	6	0.13	(1.85, 1.68)	(0.25, 2.82)		5	0.14	(1.76, 1.64)	(0.23, 2.69)
	11	0.15	(2.02, 1.61)	(0.25, 2.61)		11	0.16	(1.92, 1.57)	(0.23, 2.48)
	103	0.06	(3.78, 1.98)	(0.25, 3.93)		102	0.07	(3.66, 1.98)	(0.23, 3.91)
	1019	0.01	(9.65, 3.56)	(0.25, 12.7)		1019	0.01	(9.36, 3.48)	(0.23, 12.1)
rDNS3	0.3	0.12	(1.59, 1.70)	(0.22, 2.89)					
	5	0.14	(1.75, 1.65)	(0.22, 2.72)					
	13	0.15	(1.91, 1.61)	(0.22, 2.58)					
	105	0.06	(3.63, 2.00)	(0.22, 4.01)					
	1021	0.01	(9.32, 3.49)	(0.22, 12.2)					

Table 3. Grid resolutions for the rough-wall TBL. Here, $\epsilon^+ \equiv 2\nu\overline{\langle s_{ij}s_{ij}\rangle}^+$ where s_{ij} is the fluctuating rate of the strain tensor (Pope 2000). For the TKE transport, we denote $\epsilon''^+_K = (1/2)\epsilon^+$. Here, $\eta^+ \equiv (\epsilon^+)^{-1/4}$ is the Kolmogorov length scale, and $t^+_\eta \equiv (\epsilon^+)^{-1/2}$ is the Kolmogorov time scale.

of a boundary layer. The shape factor converges at approximately $x/\delta^*_0 \geq 2500$ or equivalently at approximately $Re_\tau \geq 1700$, indicating a fully developed turbulent state. The root-mean-square roughness height is defined as

$$h^2_{rms} = \frac{1}{A_{xz}} \iint (h_k(x,z) - h_m)^2 \,\mathrm{d}x\,\mathrm{d}z, \tag{2.2}$$

where $A_{xz} = L_xL_z$ is the roughness surface area and $h_m = h_0$ is the roughness mean height. The average height of the roughness is defined as

$$h_a = \frac{1}{A_{xz}} \iint |h_k(x,z) - h_m| \,\mathrm{d}x\,\mathrm{d}z. \tag{2.3}$$

For three-dimensional sinusoidal surfaces, h_a is simply linked to the root-mean-square roughness height as $h_a = (4/\pi^2)h_0 = (8/\pi^2)h_{rms}$. The parameter that defines the steepness of the roughness topography is the effective slope. For three-dimensional roughness, the effective slope can be defined as (Napoli, Armenio & De-Marchis 2008; Chan *et al.* 2015; Ma *et al.* 2020)

$$ES = \frac{1}{A_{xz}} \iint |\partial_x h_k(x,z)| \,\mathrm{d}x\,\mathrm{d}z. \tag{2.4}$$

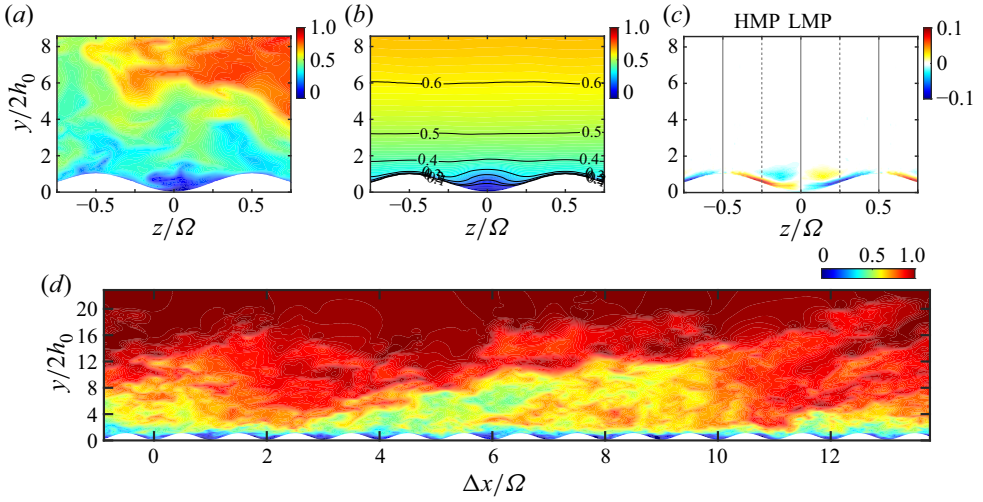

Figure 2. Realisations of rough-wall TBL. (*a*) Instantaneous streamwise velocity contour u/U_∞ (normalised by the free stream velocity U_∞) at $Re_\tau = 2820$ ($x/\delta_0^* = 6500$). (*b*,*c*) Time-averaged streamwise velocity contour (and isolines) $\bar{u}/U_\infty$ and time-averaged streamwise vorticity contour $\bar{\omega}_x^+$ at $Re_\tau = 2820$ ($x/\delta_0^* = 6500$). High-momentum paths (HMP) and low-momentum paths (LMP) are indicated by dashed and solid lines, respectively. (*d*) Instantaneous streamwise velocity u/U_∞ (flow from left to right) at $x/\delta_0^* = 2780 - 3075$ ($Re_\tau \approx 1700$), $z/\delta_0^* = 130$.

The effective slope is used to characterise the geometry of irregular roughnesses. It is shown that the effective slope relates to the solidity parameter Λ such that $ES = 2\Lambda$ (Napoli *et al.* 2008). The solidity is the ratio between the total projected frontal roughness area and the wall-parallel projected area (Napoli *et al.* 2008; Macdonald *et al.* 2016; Forooghi *et al.* 2017) (and for a smooth-wall $\Lambda = 0$). For regular roughness, the effective slope accounts for the streamwise periodicity of the roughness pattern and the roughness height. In the present case, $ES = (8k/\pi\Omega)$.

2.3. *Velocity decomposition*

In addition to the velocity fluctuation obtained based on the Reynolds decomposition. The velocity fluctuation is also obtained based on the triple decomposition (also known as the double-averaging procedure) (Raupach & Shaw 1982; Nikora *et al.* 2001). The triple decomposition differs from the Reynolds decomposition, where the time-averaged quantity is further averaged in the spatial direction, resulting in an additional dispersive fluctuation (also known as the coherent fluctuation) representing the spatial variation of the time-averaged flow,

$$q(x, y, z, t) = \bar{q}(x, y, z) + q'(x, y, z, t), \tag{2.5}$$

$$q(x, y, z, t) = \langle\bar{q}\rangle(x, y) + q'(x, y, z, t) + \tilde{q}(x, y, z), \tag{2.6}$$

where q represents an instantaneous fluid-defined flow variable; $\bar{q}$ denotes the time-averaged value; q' denotes the corresponding fluctuation (i.e. turbulent fluctuation) based on the Reynolds decomposition (2.5); and $\tilde{q}$ denotes the corresponding dispersive fluctuation. The $\langle\cdot\rangle$ denotes a spatial-averaging procedure,

$$\langle\bar{q}\rangle(x, y) = \frac{1}{L_{z,f}(x, y)} \int_{z,f} \bar{q}(x, y, z)\, \mathrm{d}z, \tag{2.7}$$

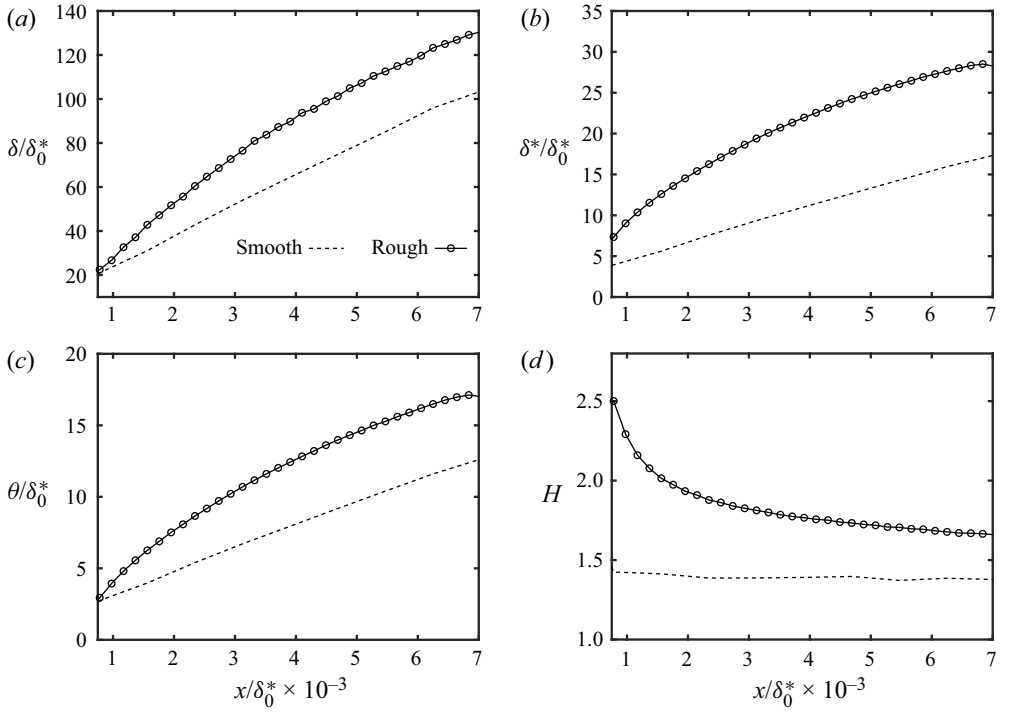

Figure 3. Global averaged boundary layer parameter variations in the streamwise direction between smooth-wall and rough-wall cases: (*a*) boundary layer thickness δ; (*b*) displacement thickness δ^*; (*c*) momentum thickness θ; and (*d*) shape factor H.

where $L_{z,f}$ is the spanwise width occupied by fluid and $0 < L_{z,f}(x, y)/L_z \leq 1$. Accordingly, the dispersive fluctuation $\tilde{q}$ represents the induced-spatial variation of the time-averaged flow due to the presence of roughness. From the triple decomposition (2.6) let $q = u_i$, the total velocity fluctuations can be defined as

$$u_i''(\boldsymbol{x}, t) = u_i'(\boldsymbol{x}, t) + \tilde{u}_i(\boldsymbol{x}), \tag{2.8}$$

where, by definition, $\overline{u_i''} = \tilde{u}_i$, and the Reynolds (turbulent) stress tensor $\overline{u_i' u_j'}$ can be written as (e.g. Türk *et al.* 2014; Vanderwel *et al.* 2019; Ma *et al.* 2021)

$$\overline{u_i' u_j'}(\boldsymbol{x}) = \overline{u_i'' u_j''}(\boldsymbol{x}) - \tilde{u}_i \tilde{u}_j(\boldsymbol{x}), \tag{2.9}$$

where, on the right-hand side of (2.9), the first term represents the total stress tensor, and the second term represents the dispersive stress tensor.

2.4. *Friction velocity estimation*

There are several direct and indirect methods for computing the friction velocity u_τ values. The direct method is based on the streamwise and wall-normal components of the mean momentum equation by assuming that the boundary layer is two-dimensional. The integrated mean momentum equation can be solved numerically and is generally suitable for data collected from numerical simulations with sufficient streamwise measurements.

The mean momentum integral equation reads as (Brzek *et al.* 2007)

$$\tau_w(x) = \nu \partial_y \bar{u}\big|_{y_a} - \overline{u'v'}\Big|_{y_a} + \int U_\infty \partial_x U_\infty \, \mathrm{d}y - \int \partial_x(\overline{u'u'}) - \partial_x(\overline{v'v'}) \, \mathrm{d}y - \int \partial_x(\bar{u}\,\bar{u}) \, \mathrm{d}y - \bar{u}\,\bar{v}|_{y_a}, \tag{2.10}$$

for an arbitrary chosen wall-normal location $y_a > e$. The friction velocity based on the mean wall shear stress is defined as

$$(u_\tau/U_\infty)^2 = (\tau_w/(\rho U_\infty^2))^2 = C_f/2. \tag{2.11}$$

A limitation of this method is that it is computationally more costly than most other methods, especially for the DNS of TBL. Apart from the direct approach, there are also several indirect approaches to compute the friction velocity. Many indirect approaches often require much fewer flow measurements, especially when the near-wall measurement is not available, and thus are commonly used for numerical and experimental data sets. The modified Clauser method computes the friction velocity by fitting the rough-wall data to an assumed log-law region of the mean velocity profile (Perry & Li 1990). A limit is that the choice of u_τ and virtual origin of the wall might not be unique at low Reynolds numbers. Another possible method is based on the assumption of outer-layer similarity (see e.g. Monty *et al.* 2011). From this approach, one first computes a pair of initial values for the friction velocity and virtual wall offset based on the modified Clauser method. Then, one assumes that the outer-layer similarity holds for the mean velocity and streamwise velocity fluctuation intensity profile under outer scaling and systematically fits the rough-wall data to the smooth-wall data and minimises the combined difference for a range of u_τ. Subsequently, the assumption of outer-layer similarity is checked by plotting outer-scaled data using the assumed friction velocity and virtual wall origin. The argument implies that the outer-layer similarity hypothesis is invalid if outer-scaled data do not collapse well. Recently, Kumar & Mahesh (2022) proposed an indirect method to determine the wall shear stress based on a mean stress model (Kumar & Mahesh 2021). This method does not require near-wall measurements and is applicable to both smooth- and rough-wall TBL. In this study, the friction velocity is computed based on the mean stress model. The friction velocity is recast as

$$u_\tau = \frac{1}{\zeta_1 - \zeta_0} \int_{\zeta_0}^{\zeta_1} \left\langle \sqrt{\frac{\Theta(\zeta)}{1 - \bar{u}(\zeta)\bar{v}(\zeta)/U_e V_e}} \right\rangle \mathrm{d}\zeta, \tag{2.12}$$

where Θ is the sum of viscous stress and Reynolds shear stress, $\zeta = y_e/\delta$, $U_e = \bar{u}(y_e = \delta)$ and $V_e = \bar{v}(y_e = \delta)$, where $y_e^+ = (y^+ - e^+)$, and e is offset from the reference virtual plane for rough-wall TBL (table 2). In the present study, the offset is defined as the location of the zero mean streamwise velocity at the farthest point from the wall: a condition that is also satisfied by the no-slip condition at the surface of the smooth-wall case. The boundary layer thickness is thus defined as $\delta = \langle y(\bar{u} = 0.99U_\infty) - y(\bar{u} = 0)\rangle$ or $\delta = \langle y(\bar{u} = 0.99U_\infty) - e\rangle$. In this paper $\zeta_1 = 0.35$ and $\zeta_0 = 0.2$ are used based on ideal values according to Kumar & Mahesh (2022). We define the friction velocity based on this method as it does not require an adjustment to account for wall roughness and has been shown to be robust over a range of Reynolds numbers for both smooth- and rough-wall ZPG TBL (Kumar & Mahesh 2022). It is relatively insensitive to the choice of the virtual origin of the wall, the shape factor H and the size of the data set. It is, therefore, suitable

Case	$u_{\tau,1}/U_\infty$	e_1^+	$l_{s,1}^+$	$u_{\tau,2}/U_\infty$	e_2^+	$l_{s,2}^+$
rDNS1	0.0526	23.7	5.05	0.0524	33.6	4.24
rDNS2	0.0502	22.6	4.66	0.0510	36.2	4.23
rDNS3	0.0499	22.5	4.88	0.0508	36.6	4.48

Table 4. Friction velocity estimation based on the mean stress model ($u_{\tau,1}$) (Kumar & Mahesh 2022) and CSS method ($u_{\tau,2}$) (Womack *et al.* 2019). Here, $l_{s,1}^+$ and $l_{s,2}^+$ denote the roughness length estimated based on $(u_{\tau,1}, e_1^+)$ and $(u_{\tau,2}, e_2^+)$, respectively.

for the current data set, and a robust friction velocity value can be obtained at a reasonable computational expense.

Additional comparisons between the friction velocity $u_{\tau,1}$ obtained based on the mean stress model (Kumar & Mahesh 2022) and the comprehensive shear stress (CSS) method (Womack, Meneveau & Schultz 2019) are presented. Unlike the mean stress model, the CSS method is an iterative method based on the rescaled mean momentum integral equation and the log-law equation. To determine the friction velocity, $u_{\tau,2}$, the total shear stress balance was first fitted in the range $0.15 < (y - e_2)/\delta < 0.3$, where $\delta = \langle y(\bar{u} = 0.99U_\infty) - e_2\rangle$. The log-law equation was then fitted in the range $0.07 < (y - e_2)/\delta < 0.15$ to estimate the roughness length $l_{s,2}$ and the wall offset e_2 (Volino & Schultz 2018; Womack *et al.* 2019, 2022). Table 4 shows the friction velocity computed based on the mean stress model and the CSS method. Overall, the mean stress model consistently yields similar results to the CSS method. It was also checked that the small discrepancy in the actual value of friction velocity does not affect the inner-scaled profiles discussed in the results section. Therefore, in the results section, the friction velocity is based on the mean stress model. The u_τ values computed based on (2.12) for the rough-wall cases are listed in table 2.

3. Results and discussion

3.1. *Mean velocity flow*

The mean velocity profile in rough-wall flow relating to the roughness Reynolds number k^+ is expected to follow the log-law profile in the form of

$$\langle \bar{u} \rangle^+ = U^+ = \frac{1}{\kappa} \ln(y_e^+) + B - \Delta U^+, \tag{3.1}$$

where the von Kármán constant is $\kappa = 0.384$, the smooth-wall intercept is $B = 4.17$ (Marusic *et al.* 2013; Womack *et al.* 2022). Here ΔU^+ is the Hama roughness function that measures the downward shift in the log law region compared with the smooth-wall case (Hama 1954). Figure 4(*a*) presents the inner-scaled mean velocity profiles for the rough-wall TBL and smooth-wall TBL. The mean velocity profiles of the rough-wall TBL at three different Reynolds numbers clearly present a constant downward shift in the logarithmic overlap region compared with smooth-wall TBL. The rough-wall profiles exhibit a log–linear region with a slope of approximately $1/\kappa$ between approximately $200 \leq y_e^+ \leq 400$. The roughness function ΔU^+, is thus determined based on (3.1) at $y_e^+ \simeq 200 - 400$ with the inner-scaled profile for the smooth-wall case. This gives $\Delta U^+ \simeq 8.3$ for rough-wall cases rDNS1, rDNS2 and rDNS3, indicating that all the rough-wall cases are in the fully rough regime. The roughness function associated with the present sinusoidal roughness is greater than that observed for cube roughness (Lee *et al.* 2011).

The difference in the roughness function can be attributed to various roughness parameters, including the roughness aspect ratio, effective slope and skewness factor. Previous studies have also shown that the roughness function is indeed influenced by the k^+ and Reynolds number for both irregular and regular surfaces. Specifically, the roughness effects tend to increase with the friction Reynolds number and k^+ (Chan *et al.* 2015; Busse *et al.* 2017; Ma *et al.* 2020). Notably, investigations conducted by Volino *et al.* (2011) and Lee *et al.* (2011) on cubical roughness have provided evidence of the dependence on k^+ and Re_τ, which is associated with an increasing roughness function. Similar observations have been made for three-dimensional sinusoidal roughness in turbulent channel flows, as demonstrated in the study by Ma *et al.* (2020). Since the present case is in the fully rough regime (Flack & Schultz 2010), the equivalent sand grain roughness, $k_s^+ = k_s u_\tau/\nu$, is estimated based on the $\Delta U^+ - k_s^+$ relationship as

$$\ln k_s^+ = \kappa(\Delta U^+ + 8.5 - B), \tag{3.2}$$

for the collapsing of rough surfaces in the fully rough regime where $\Delta U^+ > 7.0$ (Flack & Schultz 2010) and this gives $k_s^+ \simeq 128$ for all rough-wall cases. The equivalent sand grain roughness is a common roughness length scale used to compare the roughness function between different types of roughness flows with uniform sand grains by Nikuradse (1933). In addition, we obtain the relationship $k_s^+ \simeq 3.2k^+$ for the present sinusoidal roughness. This value is slightly smaller than those reported by Chan *et al.* (2015) and Ma *et al.* (2020) for three-dimensional sinusoidal roughness. Figure 4(*b*) presents the mean velocity profile in a velocity-defect form where the flow similarity in the outer part of the boundary layer can be observed, suggesting that the direct influence of roughness is mainly confined to the roughness sublayer, $y_e^+ < y_r^+$, where the roughness sublayer is typically assumed to have a wall-normal extent of five times of the roughness height or $y_r^+ \leq 5(k^+)$ (Jiménez 2004; Lee *et al.* 2011; Chung *et al.* 2021). The flow similarity manifests as outer-layer or wall similarity (Townsend 1956), which states that in the outer region of the flow, regardless of smooth or rough surface conditions, the turbulent motion is independent of the surface condition and that implies mean flow and turbulent statistics agree well between smooth- and rough-wall cases in the outer region of the flow (Raupach *et al.* 1991; Chung *et al.* 2021; Kadivar *et al.* 2021). The mean defect velocity profiles in TBLs over various roughness types are plotted in figure 4(*b*) for comparison. The mean defect velocity profiles also exhibit similarity in the outer region when compared with profiles obtained for staggered cubes, transverse rods and bars. The equivalent sand grain roughness k_s^+ ranges from the transitionally rough regime, $k_s^+ = 57.9$ for staggered cubes (Lee *et al.* 2011) to the fully rough regime, $k_s^+ = 755$ for large bars (Volino *et al.* 2011). This similarity suggests that the mean flow may be minimally affected by the differences in roughness types between sinusoidal and cubical rough surfaces.

3.2. *Reynolds and dispersive stresses*

Figure 4(*c*,*d*) shows profiles of the Reynolds shear stress and dispersive shear stress obtained by (2.9) and plotted in inner and outer coordinates. Figure 4(*c*) shows that for the Reynolds shear stress, the Reynolds number effect (the Reynolds number increases in the arrow direction) is seen in the outer region $y_e^+ > 10^3$, and the case rDNS2 ($Re_\tau = 2080$) collapses well to the sDNS ($Re_\tau = 2020$) because of the similar Reynolds numbers. The Reynolds number effect is small when plotting the Reynolds shear stress in outer coordinates, as shown in figure 4(*d*). The Reynolds shear stress profile is further compared across the present roughness type and various other roughness types in figure 4(*d*). The evidence of outer-layer similarity is less pronounced in the Reynolds shear stress profile,

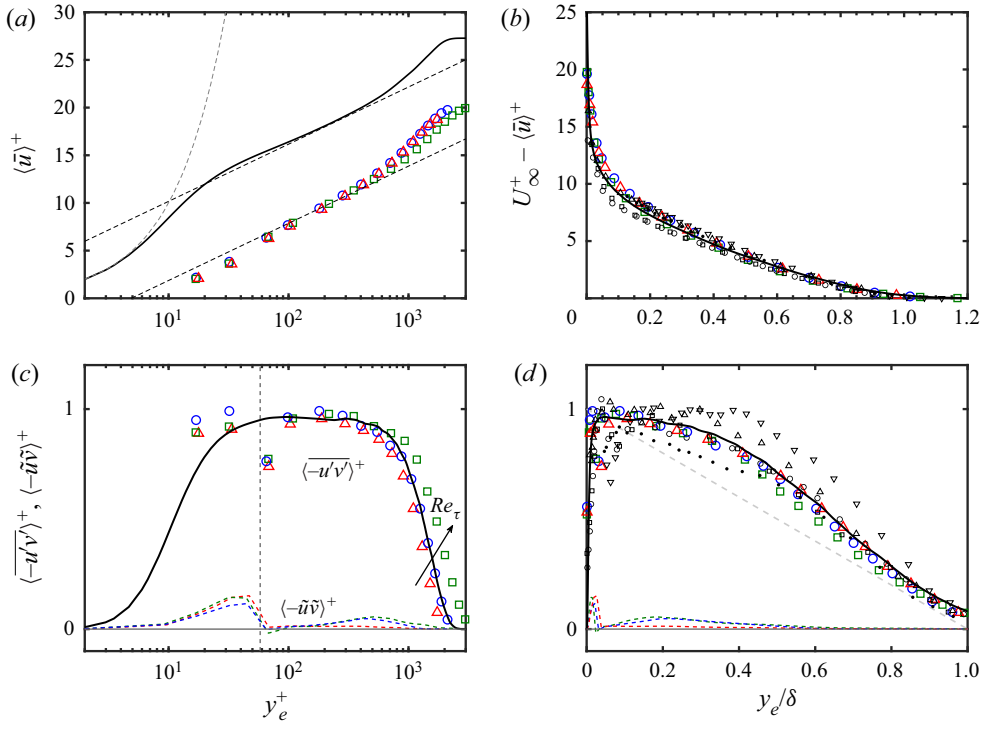

Figure 4. (*a*) Mean streamwise velocity profile and (*b*) mean velocity defect profile. Coloured symbols are rDNS1 (red △), rDNS2 (blue ○), rDNS3 (green □). Solid black line is sDNS. The dashed lines for the sDNS case denote linear $\langle \bar{u} \rangle^+ = y^+$ and log-law region $\langle \bar{u} \rangle^+ = 1/\kappa \log y^+ + C$ with $\kappa = 0.384$, $C = 4.17$. (*c*, *d*) Profiles of Reynolds shear stress $\langle -\overline{u'v'} \rangle^+$ and dispersive shear stress $\langle -\tilde{u}\tilde{v} \rangle^+$ in (*c*) inner and (*d*) outer coordinates. Dashed lines denote the dispersive shear stress for rDNS1 (red), rDNS2 (blue), rDNS3 (green). The vertical dashed line in (*c*) denotes the maximum height of the roughness, $k_e^+ = 2k^+ - e^+$ for the case rDNS1 with magnitude similar to that of rDNS2 and rDNS3. Black symbols in (*b*,*d*) are (△) small square transverse bars, (●) staggered cubes and (▽) large square transverse bars (Volino *et al.* 2011); (○) transverse rods and (□) staggered cubes (Lee, Sung & Krogstad 2011).

particularly when comparing the large square transverse bars with the other cases. This observation aligns with the findings of Volino *et al.* (2011), who noted that the outer-layer effects appear to be more prominent in the Reynolds shear stress profile of rough-wall TBLs. The difference in the outer layer may be attributed to the roughness dimensions rather than solely being a result of variations in k^+ or k/δ values. Compared with the Reynolds shear stress, the dispersive shear stress is mainly confined to the roughness sublayer. This is consistent with the observations of Poggi *et al.* (2004), Coceal *et al.* (2006), Coceal *et al.* (2007*b*) and Bailey & Stoll (2013) for flow over regular plant canopies and is similar to the observation of Ma *et al.* (2021) for random rough surfaces. The Reynolds normal stress components are plotted in figure 5.

For figure 5(*a–c*), the near-wall peak of the streamwise Reynolds stress, which is observed in the smooth-wall case, is not observed in the rough-wall cases, while the wall-normal and spanwise Reynolds stress components increase in magnitude at $100 \leq y_e^+ \leq 500$ for all cases. The increase in magnitude for the spanwise component is more pronounced than that of the wall-normal component. Overall, the variation in the streamwise turbulence intensity and the increases in the wall-normal and spanwise turbulence intensities at a matched Reynolds number are consistent with the observations

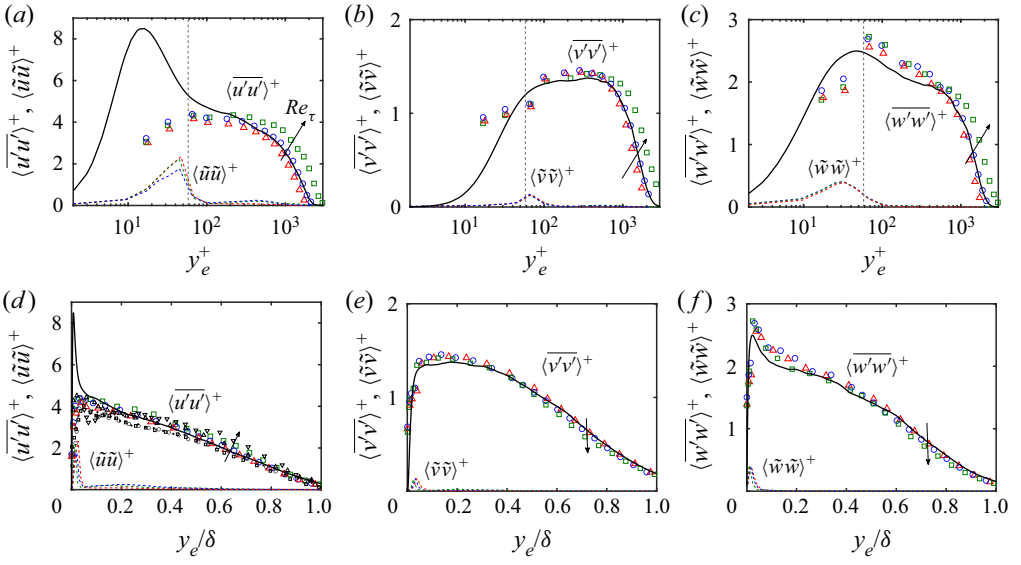

Figure 5. Reynolds and dispersive stress profiles. Legend as per figure 4.

by Krogstad & Antonia (1999) and Chan *et al.* (2015). For all Reynolds normal stress components, the rDNS2 case collapses to the sDNS case in the outer region, as the Reynolds numbers for both cases are similar. Therefore, the slight discrepancies for all three Reynolds stress components between the smooth-wall case, and the rough-wall cases rDNS1 and rDNS3, are due to the Reynolds number effect. Additionally, the dispersive normal stresses and dispersive shear stress are primarily confined to the roughness sublayer, suggesting that the secondary motion is confined within the roughness layer. For figure 5(*d–f*), similarity in the variance in the outer region between the smooth-wall case and the present rough-wall cases is observed. Interestingly, for the rough-wall cases, small Re_τ dependence may be observed, as indicated by the arrow. However, this is not observed for rough-pipe flows (Chan *et al.* 2015). The streamwise Reynolds stress profiles between the present and various previous roughness types are compared again in figure 5(*d*). A similarity is observed between most of the profiles in the outer region $y_e > 0.8\delta$ for different roughness geometries. However, for $y_e < 0.8\delta$, a noticeable deviation of the inner-scaled streamwise Reynolds stress is evident, and strongly depends on the specific roughness type.

3.3. *Linear asymptote in the diagnostic plot*

Outer-layer behaviour in the streamwise mean velocity and root-mean-square turbulent fluctuation is further examined through the diagnostic plot (Alfredsson *et al.* 2011, 2012; Alfredsson, Segalini & Örlü 2021). The diagnostic plot reveals that, at least in the case of smooth-wall ZPG TBLs, within the flow region extending from the logarithmic region and reaching almost the entire outer wake region, a linear asymptote exists between streamwise mean velocity and root-mean-square turbulent fluctuation, characterised by $\langle \overline{u'u'} \rangle^{1/2}/\langle \bar{u} \rangle = a - b\langle \bar{u} \rangle/U_\infty$, where a and b are constants obtained from smooth-wall data.

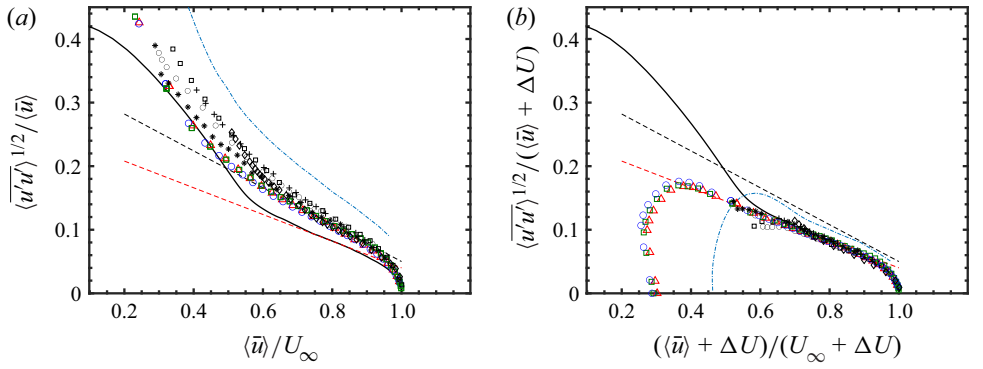

Figure 6. (*a*) Diagnostic plot of the mean streamwise velocity and root-mean-square turbulent fluctuation (Alfredsson *et al.* 2011; Alfredsson, Örlü & Segalini 2012) and (*b*) modified empirical scaling form (Castro *et al.* 2013). Solid black line: sDNS. Coloured symbols are rDNS1 (red △), rDNS2 (blue ○) and rDNS3 (green □). The red dashed line denotes linear smooth-wall asymptote, $\langle\overline{u'u'}\rangle^{1/2}/\langle\bar{u}\rangle = a - b\langle\bar{u}\rangle/U_\infty$, where $a = 0.25$, $b = 0.21$. The black dashed line denotes linear rough-wall asymptote, $\langle\overline{u'u'}\rangle^{1/2}/\langle\bar{u}\rangle = \hat{a} - \hat{b}\langle\bar{u}\rangle/U_\infty$, where $\hat{a} = 0.34$, $\hat{b} = 0.29$. Black symbols in (*a*,*b*) are (○) (Flack, Schultz & Connelly 2007), (□) (Krogstad & Efros 2012), (∗) (Brzek *et al.* 2008), (◇) (Medjnoun *et al.* 2021), (+) (Amir & Castro 2011) and (—·—·) (Forooghi *et al.* 2018).

Castro *et al.* (2013) further showed that in the case of transitional and fully rough ZPG TBLs, the rough-wall linear asymptote may also be expressed by $\langle\overline{u'u'}\rangle^{1/2}/\langle\bar{u}\rangle = \hat{a} - \hat{b}\langle\bar{u}\rangle/U_\infty$. Subsequently, Castro *et al.* (2013) proposed a modified form of the rough-wall linear asymptote, i.e. $\langle\overline{u'u'}\rangle^{1/2}/\langle(\bar{u} + \Delta U)\rangle = \hat{a} - \hat{b}\langle(\bar{u} + \Delta U)\rangle/(U_\infty + \Delta U)$. In this modified form where ΔU is the roughness function, and $\tilde{a} \simeq a, \tilde{b} \simeq b$. This suggests a universal scaling between the streamwise mean velocity and root-mean-square turbulent fluctuation, applicable to both smooth-wall and rough-wall ZPG TBLs (at least in fully rough conditions). This universality appears to be independent of the friction velocity value and the choice of wall offset (Castro *et al.* 2013).

Figure 6(*a*) displays the diagnostic plot for data sets of smooth-wall and rough-wall TBLs, including the present sinusoidal roughness cases and data sets from prior studies on rough-wall TBLs.

It can be observed that both smooth-wall and rough-wall TBLs exhibit distinct linear asymptotes. The present sinusoidal roughness cases and other rough-wall cases collapse to a rough-wall linear asymptote with $\hat{a} = 0.34$ and $\hat{b} = 0.29$ (Flack *et al.* 2007; Brzek *et al.* 2008; Amir & Castro 2011; Krogstad & Efros 2012; Castro *et al.* 2013), and the smooth-wall TBL data set aligns with a smooth-wall linear asymptote characterised by $a = 0.25$ and $b = 0.21$.

This lack of collapse between the smooth-wall and rough-wall cases is attributed to the increase in streamwise turbulent intensity, primarily due to the non-zero roughness function ΔU observed in the rough-wall cases. This finding aligns well with the observations made by Castro *et al.* (2013) and is confirmed in figure 6(*b*). In figure 6(*b*), the modified form of the diagnostic plot is presented. The inclusion of the roughness function in the modified scaling reveals a remarkable collapse starting at $(\langle\bar{u}\rangle + \Delta U)/(U_\infty + \Delta U) \simeq 0.4$. This collapse is observed among the present sinusoidal roughness cases, previous roughness cases and the smooth-wall case (Flack *et al.* 2007; Brzek *et al.* 2008; Amir & Castro 2011; Krogstad & Efros 2012; Castro *et al.* 2013). A similar argument also

holds for root-mean-square total fluctuation, as demonstrated by Medjnoun *et al.* (2021), and is depicted in figure 6.

We have also observed that the universal scaling does not apply when comparing flow data sets of different flow types. The discrepancy is illustrated by including a turbulent channel case studied by Forooghi *et al.* (2018). There is no collapse observed between all the rough-wall ZPG TBL cases and the turbulent channel case. Notably, prior findings reported had consistently identified universal behaviour within channel results (Forooghi *et al.* 2018; Stroh *et al.* 2020).

The analysis provides partial evidence of the universal outer-layer behaviour in the diagnostic plot between smooth-wall and rough-wall TBLs when modified to account for the ΔU. Consequently, ΔU appears to play a significant role in generating the linear collapse in the outer region between smooth-wall and rough-wall TBLs despite the different roughness morphologies and turbulence structures in the outer region of smooth-wall and rough-wall TBLs.

3.4. *Spanwise length scales and mean structure angles*

A comparison of turbulent structures over rough surfaces and smooth-wall-bounded flows has been undertaken using many different approaches. Examples are turbulent motions from their 'energy' contents, e.g. spectral analysis of the velocity fluctuating components and two-point correlations (Volino *et al.* 2007; Nugroho, Hutchins & Monty 2013; Nadeem *et al.* 2015; Chan *et al.* 2018) or the proper-orthogonal decomposition (Cardillo *et al.* 2013; Vanderwel *et al.* 2019; Wangsawijaya & Hutchins 2022). The spanwise length scale associated with the Reynolds normal stresses distribution is investigated here using the one-dimensional wavenumber spectrum. The one-sided wavenumber cospectrum (power spectral density) is computed by

$$\Phi_{ij}(y, k_z) = 2\overline{\left\langle \mathrm{Re}\left[\mathcal{F}[u_i'](y, k_z)\mathcal{F}[u_j']^*(y, k_z)\right]\right\rangle}, \quad k_z > 0, \tag{3.3}$$

$$\overline{\langle u_i' u_j' \rangle}(y) = \int_0^\infty \Phi_{ij}(y, k_z)\,\mathrm{d}k_z = \int_{-\infty}^\infty k_z \Phi_{ij}(y, k_z)\,\mathrm{d}(\ln k_z), \tag{3.4}$$

where $\mathcal{F}[u_i']$ is the Fourier transform of the velocity fluctuation in the spanwise direction; $\mathcal{F}[u_j']^*$ is the complex conjugate of $\mathcal{F}[u_j']$. The Re[·] is the real part of the cross-wavenumber spectral density function (Bendat & Piersol 2011). Here k_z is the spanwise wavenumber. The factor of two accounts for the expected value of the negative k_z part, which is identical to its positive k_z counterpart, and we only consider the positive wavenumber range $k_z > 0$. The expected value is taken as the ensemble averaging over all realisations. The spanwise wavelength is thus defined as $\lambda_z = 2\pi/k_z$ for $\lambda_z > 0$.

Figure 7 shows the spanwise premultiplied energy spectra between the smooth-wall and rough-wall cases with the smallest and largest Re_τ. For the streamwise velocity spectra $k_z\Phi^+_{u'u'}$ compared with the smooth-wall case as shown in figure 7(*a*,*b*), the inner peak at $\lambda_z{}^+ \simeq 100$ and $y^+ \simeq 15$ characterises the near-wall structures in the smooth-wall case and is found at higher y^+ and λ_z^+ values, suggesting that the near-wall cycle exists but is shifted above the plane of the crests with increased spanwise wavelength. This is consistent with the observations of Chan *et al.* (2018). Also, it can be seen from figure 7(*a*,*b*) that the outer peak is located at $\lambda_z \simeq 0.7\delta$ and $y \simeq 0.15\delta$, which scales with the outer variable and characterises very large-scale motions (Kim & Adrian 1999; Tomkins & Adrian 2005; Guala, Hommema & Adrian 2006; Hutchins & Marusic 2007; Monty *et al.* 2009). The outer peak suggests that differences in the location and energy contribution

in the large spanwise wavelengths are observed. This may indicate potential influences on the outer-layer motions from large spanwise wavelength structures due to roughness elements. For the energy spectra of wall-normal and spanwise velocity components, figure 7(*c–f*) suggests that, although no distinct double peaks can be observed in the profiles, more energy appears to reside at higher y_e^+ and λ_z^+ values. This seems to reflect the increased wall-normal and spanwise Reynolds stress components as observed previously in figure 5(*b*,*c*). The increase of the wall-normal Reynolds stress is likely attributed to the increase in the turbulent mixing of high-speed and low-speed fluids between the near-wall and outer regions, as observed in previous studies (Chan *et al.* 2018; Yang & Anderson 2018; Vanderwel *et al.* 2019).

The mean SIA characterises the average structure inclination angle of the wall-attached motions, which are found to be populated in the logarithmic and outer regions where they are rooted in the near-wall region and inclined at an angle to the mean flow (Marusic & Heuer 2007; Volino *et al.* 2007). The SIA is typically inferred by deducing the local maximum value of the streamwise cross-correlation function between streamwise velocity fluctuations (u') at a reference wall-normal location y_r and at a wall-normal location in the log region (y_o) (Marusic & Heuer 2007),

$$R_{u_r u}(\Delta x, y) = \frac{\langle \overline{u'(x, y_r, z) u'(x + \Delta x, y, z)} \rangle}{\sqrt{\langle \overline{u'(y_r)^2} \rangle} \sqrt{\overline{u'(y)^2}}}, \quad y \geq y_r, \tag{3.5}$$

where y_r denotes the wall-normal location in the roughness sublayer.

For smooth-wall-bounded turbulent flows, the reported range of the SIA is typically between 10° to 16° in experimental and numerical studies of ZPG TBLs, and channel flows (Marusic & Heuer 2007; Deshpande, Monty & Marusic 2019; Cheng, Shyy & Fu 2022). For rough-wall-bounded turbulent flows, the inclination angle is obtained by the least-squares fitted line using points from farthest up and downstream of the correlation peak on the contour levels from 0.4 to 0.9, centred at $y/\delta = 0.2$ and above (Volino *et al.* 2007). Figure 8 shows the angles obtained from the least-squares method for the cases rDNS1 and rDNS3 with the smallest and largest Re_τ, which are in the range 19°–21°. The angles are bounded by a wide range of values of 12°–38° reported in the literature for TBL over woven mesh and cubical roughness (Krogstad & Antonia 1994; Coceal *et al.* 2007*a*; Volino *et al.* 2007; Lee *et al.* 2011; Volino *et al.* 2011). The discrepancy can only be attributed to different roughness types. Overall, the result is generally consistent with the literature that the SIA for rough-wall-bounded flows is either higher or similar compared with a smooth wall at the same Reynolds numbers (Krogstad & Antonia 1994; Castro, Cheng & Reynolds 2006; Coceal *et al.* 2007*a*; Volino *et al.* 2007; Lee *et al.* 2011; Volino *et al.* 2011; Yuan & Piomelli 2014).

3.5. *Total stress transports*

The transports of total, Reynolds and dispersive normal stresses are investigated using the triple-decomposed kinetic energy transport equations. By introducing the triple velocity decomposition (2.6) to the incompressible Navier–Stokes equations, the transport equations for the total/turbulent/dispersive stresses are obtained by multiplying the total/turbulent/dispersive velocity fluctuations with the incompressible Navier–Stokes equations and taking the time average; then interchanging *i* and *j* components and summing up the resulting equation. The transport equations for total/turbulent/dispersive stresses are

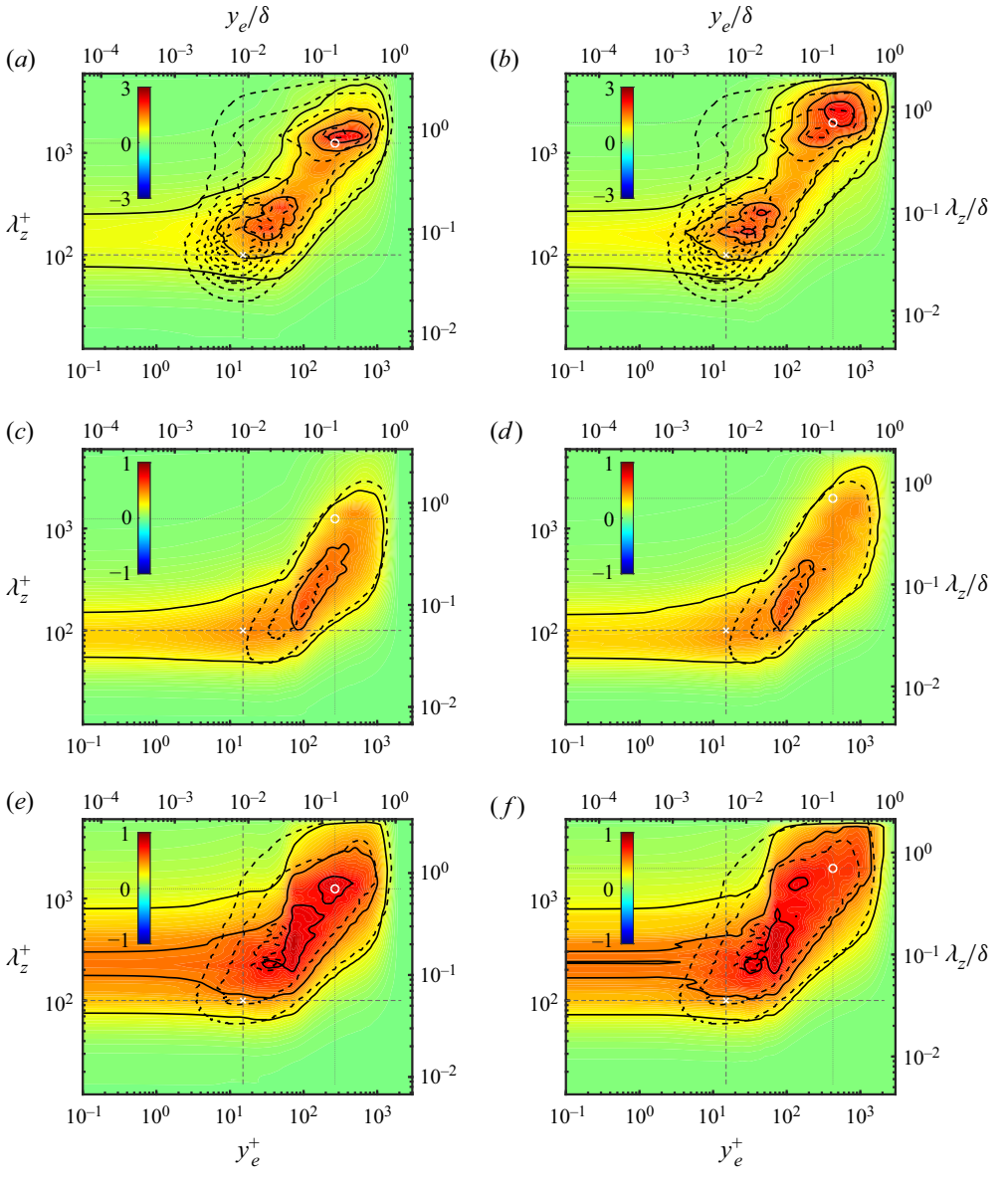

Figure 7. One-dimensional spanwise wavenumber premultiplied energy spectra: (*a*,*c*,*e*) rDNS1 ($Re_\tau = 1780$, $x = 3000\delta_0^*$) and (*b*,*d*,*f*) rDNS3 ($Re_\tau = 2820$, $x = 6500\delta_0^*$). (*a*,*b*) Streamwise velocity $k_z\Phi^+_{u'u'}$, (*c*,*d*) wall-normal velocity $k_z\Phi^+_{v'v'}$ and (*e*,*f*) spanwise velocity $k_z\Phi^+_{w'w'}$ components for (colour and solid contours lines) rDNS cases and (dashed contour lines) sDNS case. The contour levels are (*a*,*b*) 0.5[0.5]2, (*c*,*d*) 0.25 and 0.5, (*e*,*f*) 0.25, 0.5 and 0.75, respectively. The white symbol × marks the classic near-wall peak and the white symbol ○ marks the outer peak observed in $k_z\Phi^+_{u'u'}$ of the sDNS case.

obtained as (refer to Appendix A)

$$C''_{ij} = P''_{ij} + D''_{ij} + \Pi''_{ij} + D''_{\nu,ij} - \epsilon''_{ij}, \tag{3.6}$$

$$C'_{ij} = P'_{ij} + D'_{ij} + T_{ij} + \Pi'_{ij} + D'_{\nu,ij} - \epsilon'_{ij}, \tag{3.7}$$

$$\tilde{C}_{ij} = \tilde{P}_{ij} + \tilde{D}_{ij} - T_{ij} + \tilde{\Pi}_{ij} + \tilde{D}_{\nu,ij} - \tilde{\epsilon}_{ij}. \tag{3.8}$$

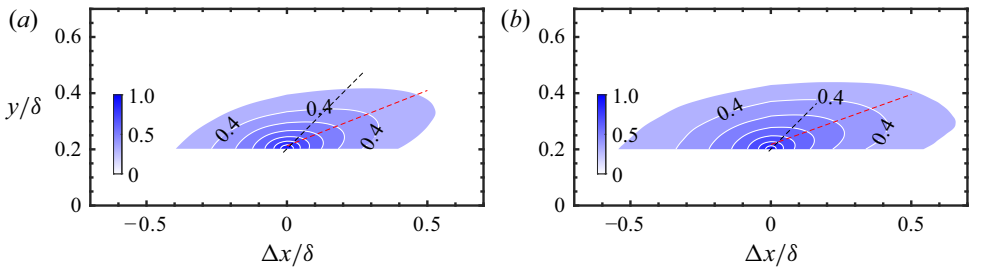

Figure 8. Cross-correlation between $u'(y_r)$ $(y_r/\delta = 0.2)$ and $u'(y)$ for (a) rDNS1 and (b) rDNS3. The inclination angle is defined as the least-squares fit from points farthest away from the self-correlation peak at contour levels from 0.4 to 0.9 with increment of 0.1 (Volino, Schultz & Flack 2007), which is highlighted as red dashed lines. Solid white lines are contour levels in increments of 0.1. Black dashed lines highlight the Δx_p corresponding to the streamwise inclination angle (SIA) $\theta_m^w = \arctan((y_o - y_r)/\Delta x_p) = 45^\circ$.

The capital letters from left to right are, respectively, C_{ij} convection tensor, P_{ij} production tensor, D_{ij} turbulent diffusion tensor, Π_{ij} velocity-pressure gradient tensor, $D_{\nu,ij}$ viscous diffusion tensor and ϵ_{ij} dissipation tensor. The notations $(\overline{\cdot})$, $(\cdot)'$ and $(\tilde{\cdot})$ denote total, turbulent and dispersive components, respectively. It can easily be verified that the sum of (3.7) and (3.8) is equal to (3.6) (refer to Appendix A). Equation (3.7) is the Reynolds stress transport equation when the dispersive stress tensor is negligible (Rotta 1951; Tennekes & Lumley 1972; Pope 2000). In (3.7) and (3.8), in addition to the terms that are reminiscent of those in (3.6), i.e. convection, production, turbulent diffusion, viscous diffusion, velocity-pressure gradient and viscous dissipation, the additional term T_{ij} is found in both (3.7) and (3.8) of opposite sign. One can interpret this term as an intercomponent transfer between Reynolds and dispersive stresses. To obtain the transport equations for total, turbulent and dispersive kinetic energy components (i.e. the sum of the normal stresses), we let $i = j$ in (3.6), (3.7) and (3.8) and multiplied the equations by $1/2$. We simplified the analysis by averaging quantities in the spanwise direction and defined the averaged form of the kinetic energy components as

$$K''(x,y) = \frac{1}{2}\langle\overline{u_i''^2}\rangle = \underbrace{\frac{1}{2}\langle\overline{u_i'^2}\rangle}_{K'} + \underbrace{\frac{1}{2}\langle\tilde{u}_i^2\rangle}_{\tilde{K}}, \tag{3.9}$$

where K'', K' and $\tilde{K}$ are functions of the streamwise and wall-normal coordinates (x, y). Here, the Einstein summation convention is assumed. We denote TKE and dispersive kinetic energy as K' and $\tilde{K}$, respectively. The K'' is the sum of the K' and $\tilde{K}$ and represents the total fluctuating kinetic energy apart from the mean flow kinetic energy.

Profiles of the K'', K' and $\tilde{K}$ transport terms of the rough-wall cases are plotted in figure 9 and are compared with the K' transport equation of the smooth-wall case. The inset plots are the same profiles plotted in outer coordinates. For the rough-wall cases, the peak production of K' is shifted towards $y_e^+ \simeq k_e^+$, where the maximum roughness height $k_e^+ = 2k^+ - e^+$ is defined for rDNS1, which is similar to that for rDNS2 and rDNS3. The peak production of K' that usually occurs within the viscous buffer layer $y^+ \simeq 11$ (smooth-wall case) is weakened in the presence of the rough wall. The location of the peak of $P_K'^+$ suggests that the mean shear is strongest near the crest of the roughness elements. As expected, the roughness influences the location of the peak mean shear at the near wall region, which is commonly observed in previous studies on turbulent rough-wall flows (e.g. Coceal *et al.* 2006; Ganju, Bailey & Brehm 2022). Because the

mean flow velocity over the roughness crest is relatively high while the mean flow velocity below the roughness is relatively much slower, the differences in the mean flow velocity result in a substantial shear near the roughness crests. The strong shear near the crests also contributes to the production of $\tilde{K}$, which occurs locally at $0 < y_e^+ \lesssim 2k_e^+$. The magnitude of the production of $\tilde{K}$ is much smaller than that of the production of K', but the location of the peak $\tilde{P}_K^+$ matches with the peak $P_K'^+$ observed at $y_e^+ \simeq k_e^+$ where the peak mean shear occurs. When the profiles are plotted in outer coordinates as shown in the inset plots, the $P_K'^+$ for all rough wall cases clearly show similar rates as the smooth-wall case and collapse onto the smooth-wall profile reasonably well for $y_e/\delta > 0.1$, while the $\tilde{P}_K^+$ occurs locally at the roughness sublayer, i.e. $y^+ = O(k^+)$ and decreases to zero above the roughness sublayer.

The viscous dissipation of K', or $\epsilon_K'^+$ in brief, has a local minimum at the $y_e^+ \simeq k_e^+$ that matches the wall-normal location of the peak shear of production (peak $P_K'^+$). We also noted that very close to the wall $y_e^+ < 0$ (not shown for brevity), the viscous diffusion ($D_{\nu,K}'^+$) and $\epsilon_K'^+$ approach a balance, where $\epsilon_K'^+$ has a global minimum. The imbalance between $P_K'^+$ and $\epsilon_K'^+$ across $y_e^+ \lesssim 2k_e^+$ is associated with the four different transport terms that act as the local sources and sinks (i.e. C_K', D_K', T_K and $D_{\nu,K}'$). In the inset plots, the profile of $\epsilon_K'^+$ collapses well to the smooth-wall profile in the outer coordinate $y_e/\delta > 0.1$.

Compared with $\epsilon_K'^+$, it is interesting to note that the dissipation of $\tilde{K}(\tilde{\epsilon}_K^+)$ has a global minimum at a similar wall-normal location $y_e^+ \simeq k_e^+$, suggesting both the production and dissipation of $\tilde{K}$ ($\tilde{P}_K^+$ and $\tilde{\epsilon}_K^+$) occur locally at $0 < y_e^+ \lesssim 2(k_e^+)$. This also suggests that $\tilde{K}$ is typically a local phenomenon within the roughness sublayer due to localised strong mean shear in the vicinity of the roughness crests.

For the rough-wall cases, the spatial transport term ($D_K'^+$) is more pronounced at a higher wall-normal location. The $D_K'^+$ has a local minimum at $y_e^+ \simeq k_e^+$, therefore acting as a local sink of K' to redistribute energy from local production towards the wall region where the local dissipation rate is higher than the local production rate, i.e. $y_e^+ \lesssim 7$ (i.e. including also $y_e^+ < 0$ where the dissipation $\epsilon_K'^+$ reaches a global minimum). Moreover, the dispersive spatial transport term ($\tilde{D}_K^+$) has a global maximum at around $y_e^+ \simeq k_e^+$, which acts as a local source of $\tilde{K}$ to balance the convection and intercomponent transfer terms, as shown later in this section.

The spatial transport term D_K' can be expressed as a sum of three terms

$$D_K'(x,y) = \underbrace{-\frac{1}{2}\left\langle \partial_k(\overline{u_i'u_i'u_k'})\right\rangle}_{D_{K,1}'} \underbrace{-\frac{1}{2}\left\langle \partial_k(\overline{u_i'u_i'}\tilde{u}_k)\right\rangle}_{D_{K,2}'} \underbrace{-\frac{1}{2}\left\langle [2\partial_k(\overline{u_i'u_k'}\tilde{u}_i)]\right\rangle}_{D_{K,3}'}, \tag{3.10}$$

and the dispersive spatial transport term $\tilde{D}_K$ can be expressed as

$$\tilde{D}_K(x,y) = -\frac{1}{2}\left\langle \partial_k(\tilde{u}_i\tilde{u}_i\tilde{u}_k)\right\rangle . \tag{3.11}$$

From the decomposition (3.10), the $D_{K,1}'$ is the turbulent spatial transport term in the classic Reynolds stress transport equation and ($\overline{u_i'u_i'u_k'}$) denote the spatial fluxes of Reynolds stresses (Pope 2000). Here $D_{K,2}'$ and $D_{K,3}'$ are additional terms that represent the turbulent-dispersive spatial transport in each direction x_k by the turbulent-dispersive spatial fluxes:($\overline{u_i'u_i'}\tilde{u}_k$) and ($\overline{u_i'u_k'}\tilde{u}_i$), respectively. The additional terms $D_{K,2}$ and $D_{K,3}$

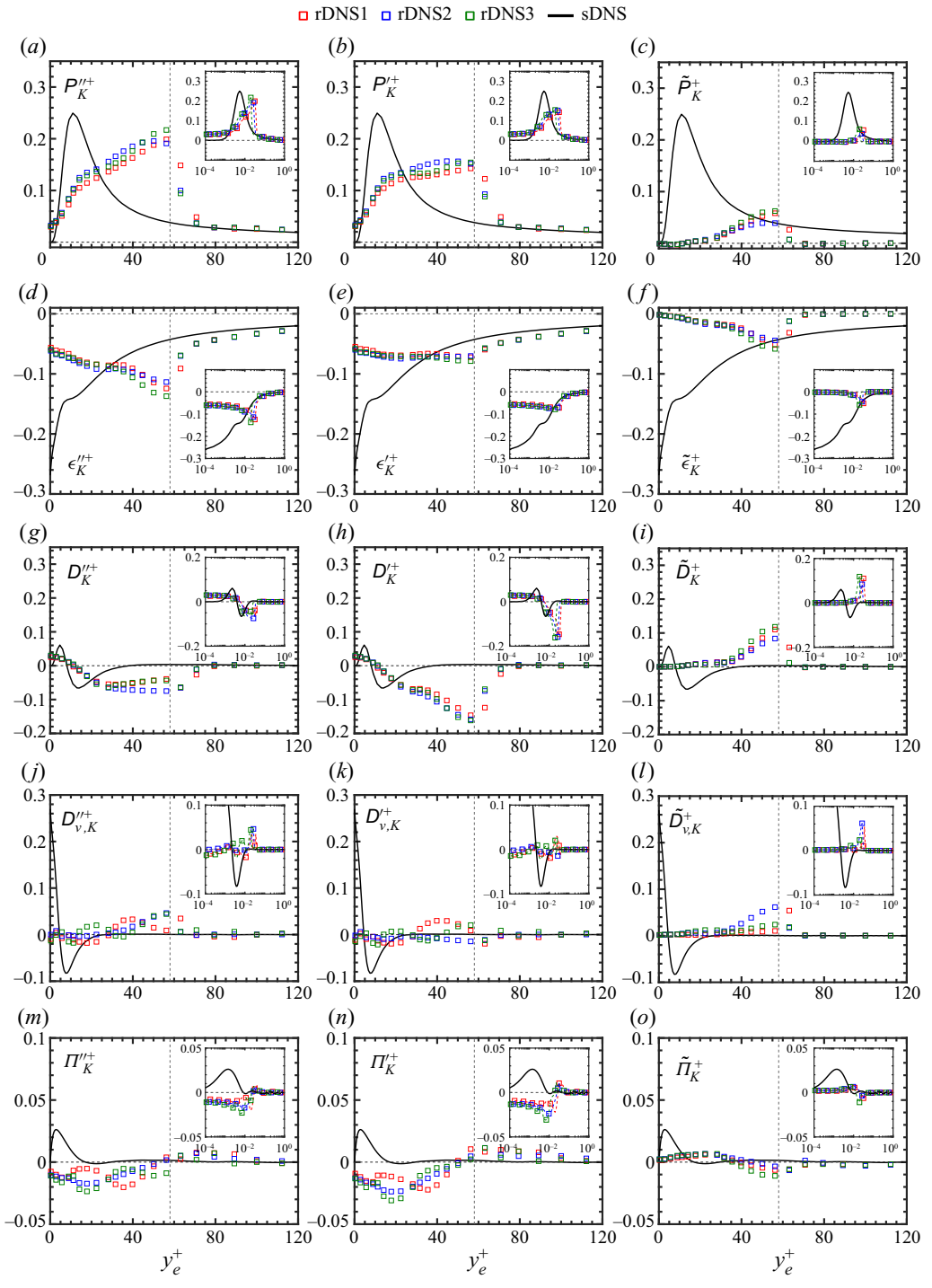

Figure 9. Profiles of the terms in the transport equations for K'' (3.6), K' (3.7) and $\tilde{K}$ (3.8). Here, P_K is the production term; ϵ_K is the dissipation term; D_K and $D_{v,K}$ are the diffusion terms; Π_K is the velocity-pressure gradient. The notations ($''$), ($'$) and ($\tilde{\cdot}$) denote total, turbulent and dispersive components, respectively. Vertical dashed line indicates the height of the roughness, $k_e^+ = 2k^+ - e^+$. Solid black lines (——) denote the terms based on (3.6) for the reference smooth-wall case. Each inset plot shows same profile plotted in outer coordinate y_e/δ.

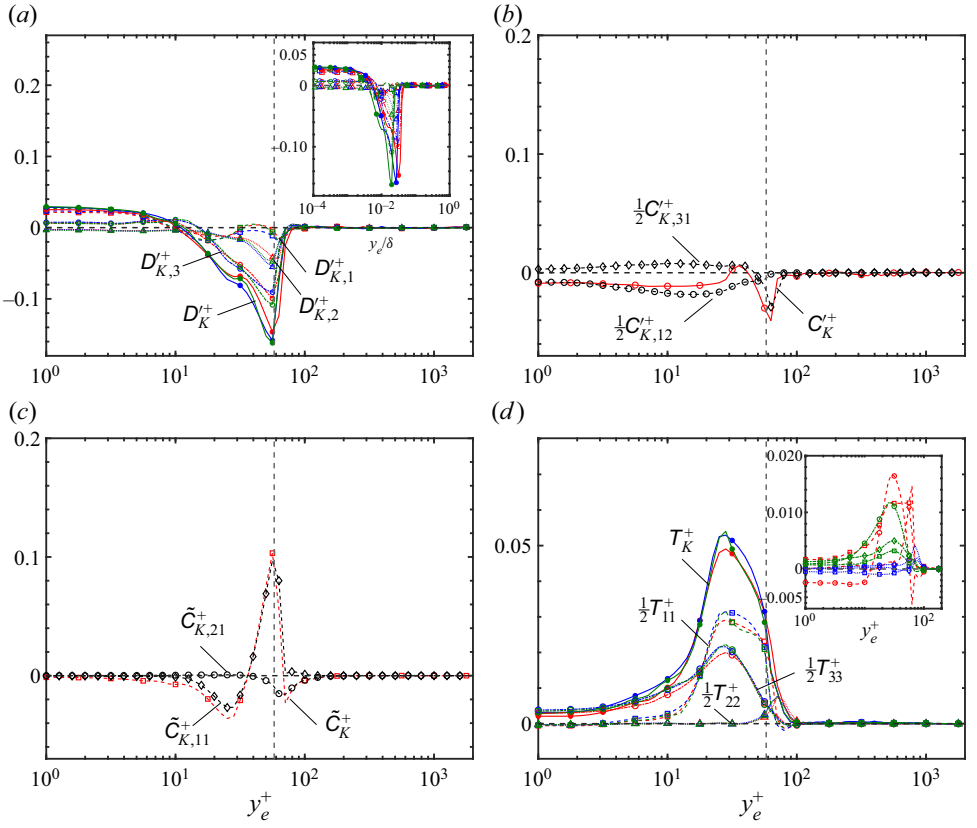

Figure 10. Profiles of the (*a*) diffusion terms D'_K based on decomposition (3.10): rDNS1 (red); rDNS2 (blue); rDNS3 (green). The inset plot shows the same profile plotted in outer coordinate. (*b*,*c*) The convection terms C'_K and $\tilde{C}_K$ for case rDNS1. (*d*) The inter-transport term T_K: (red) rDNS1; (blue) rDNS2; (green) rDNS3. Inset plot shows terms composed of T_K in the case rDNS1, where the symbols are red ($\diamond$) $\tilde{u}(\overline{u'\partial_x u'})$, ($\circ$) $\tilde{u}\partial_y(\overline{v'\partial_y u'})$, ($\square$) $\tilde{u}\,(\overline{w'\partial_z u'})$; blue ($\diamond$) $\tilde{v}(\overline{u'\partial_x v'})$, ($\circ$) $\tilde{v}(\overline{v'\partial_y v'})$, ($\square$) $\tilde{v}(\overline{w'\partial_z v'})$; green ($\diamond$) $\tilde{w}(\overline{u'\partial_x w'})$, ($\circ$) $\tilde{w}(\overline{v'\partial_y w'})$, ($\square$) $\tilde{w}(\overline{w'\partial_z w'})$. The vertical dashed line denotes the height of the roughness, $k_e^+ = 2k^+ - e^+$.

appear only when $\overline{u_i''} = \widetilde{u}_i \neq 0$, this also implies that the dispersive spatial transport $\tilde{D}_K$ in (3.11) is not necessarily zero. Figure 10(*a*) shows the decomposition of D'_K based on (3.10). It is clear that the turbulent spatial transport term $D_{K,1}$ (dashed lines) and the turbulent-dispersive spatial transport term $D_{K,3}$ (dash–dotted lines) are responsible for the transport of K' from $y_e^+ \simeq k_e^+$ towards the near-wall region (i.e. $D_{K,1}$ and $D_{K,3}$ are positive for $y_e^+ < 10$). It is also noted that $D_{K,2}$ (dotted lines) is always negative below $y_e^+ \simeq k_e^+$ and acts as a local sink for transporting K'. Overall, the finding suggests that the spatial transport of TKE is strongly affected by the additional turbulent-dispersive spatial fluxes that emerge due to the roughness. Figure 10(*a*) clearly shows that the two spatial fluxes $(\overline{u_i'u_i'}\tilde{u}_k)$ and $(\overline{u_i'u_k'}\tilde{u}_i)$ (corresponding to the $D_{K,2}$ and $D_{K,3}$ terms) play a central role in the transport of K' in the rough-wall case, compared with the smooth-wall TBL case whereby the spatial transport K' is governed by the spatial fluxes $(\overline{u_i'u_i'u_k'})$.

For the rough-wall cases, the viscous diffusion term $D'^{+}_{\nu,K}$ becomes less pronounced at the near wall region ($0 < y_e^+ < 15$) compared with the smooth-wall case. Compared with $D'^{+}_{\nu,K}$, the $\tilde{D}^{+}_{\nu,K}$ acts clearly as a local source, similar to the $\tilde{D}^{+}_{K}$ as shown previously.

This suggests that the turbulent and dispersive viscous diffusion terms are important source terms for the $\tilde{K}$ transport near the crest of the roughness elements (i.e. $y_e^+ \simeq k_e^+$). On the other hand, the two pressure transport terms $\Pi_K'^+$ and $\tilde{\Pi}_K^+$ terms are relatively small compared with all other terms. This suggests that the velocity-pressure gradient correlations do not play a significant role in the K' and $\tilde{K}$ transports compared with the spatial transport terms. In the perspective of K' and $\tilde{K}$ transports for the present rough-wall TBL, the role of $\Pi_K'^+$ is a wall-normal transport of a small fraction of K' from the roughness canopy upwards to $y_e^+ \simeq k_e^+$, while the $\tilde{\Pi}_K^+$ transports a small fraction of $\tilde{K}$ from $y_e^+ \simeq k_e^+$ downwards towards the roughness canopy.

3.6. *Convection and intercomponent transfer between K' and $\tilde{K}$*

In this section, the two additional terms of interest are convection terms C_K' and $\tilde{C}_K$ and the intercomponent transfer term T_K. For the smooth-wall case, the convection term is zero and the K' balance is obtained by the remaining five terms, whilst this does not hold for the rough-wall cases.

Figure 10(*b*) shows the convection term C_K' associated with the K' transport in the rough-wall case rDNS1 (where the trends for the cases rDNS2 and rDNS3 are similar to case rDNS1). The (turbulent component) convection terms C_K' can be approximated by

$$C_K'(x,y) = \frac{1}{2}\left\langle U_k \partial_k (\overline{u_i' u_i'}) \right\rangle \approx \underbrace{\frac{1}{2}\left\langle U \partial_x (\overline{w'w'}) \right\rangle}_{C_{K,31}'} + \underbrace{\frac{1}{2}\left\langle V \partial_y (\overline{u'u'}) \right\rangle}_{C_{K,12}'}. \tag{3.12}$$

We can observe that the $C_{K,31}'$ and $C_{K,12}'$ involved in the convection term C_K' have significant and different contributions to the transport of the K'. The $C_{K,31}'$ relates to the transport of the spanwise component of the K' in the streamwise direction by the mean flow velocity U at $y_e^+ \simeq k_e^+$, and $C_{K,12}'$ relates to the transport of the streamwise component of the K' in the wall-normal direction by the secondary flow component V and contributes to the near-wall transport $y_e^+ < k_e^+$. Therefore, the convection term of K' transport can be interpreted as terms that relate the strength of the mean streamwise flow, wall-normal secondary flow, and the anisotropic distribution of the wall-parallel turbulent momentum fluxes ($\partial_x \overline{w'w'}$ and $\partial_y \overline{u'u'}$). Figure 10(*c*) shows the (dispersive component) convection term $\tilde{C}_K$ associated with the transport of $\tilde{K}$. Although $\tilde{C}_K$ is composed of multiple components, from the figure, we can clearly observe that $\tilde{C}_K$ is dominated by two terms, which can be written as

$$\tilde{C}_K(x,y) = \langle \tilde{u}_i \partial_k (U_i U_k) \rangle + \frac{1}{2}\langle U_k \partial_k (\tilde{u}_i \tilde{u}_i) \rangle \approx \underbrace{\frac{1}{2}\langle U \partial_x (\tilde{u}\tilde{u}) \rangle}_{\tilde{C}_{K,11}} + \underbrace{\frac{1}{2}\langle U \partial_x (\tilde{v}\tilde{v}) \rangle}_{\tilde{C}_{K,21}}. \tag{3.13}$$

The reduced form of $\tilde{C}_K$ in (3.13) suggests that the local streamwise inhomogeneity ($U\partial_x(\cdot)$) introduced by the surface roughness contributes to the convection of $\tilde{K}$. There is a significant variation in the streamwise gradient of the streamwise dispersive stress where $\tilde{C}_{K,11}$ is negative at $y_e^+ < 30$, and becomes positive at $y_e^+ > 30$ and peaks at $y_e^+ \simeq k_e^+$. The local maximum streamwise turbulence intensity occurs at the region close to the roughness crest height due to the wall-normal turbulent momentum transfer of high- and low-(u') speed fluids (Chan *et al.* 2015). In analogy to this observation, the present results suggest

that the variation in the streamwise gradient of the dispersive momentum flux relates to the wall-normal dispersive momentum transfer that occurs at the wall-normal location of the maximum streamwise dispersive intensity. This location corresponds to the proximity of the roughness crests, as illustrated in figure 5. The negative $\tilde{C}_{K,11}$ may be associated with the low-$(\tilde{u})$ speed region, and transports a small fraction of $\langle\tilde{u}\tilde{u}\rangle$ from below the crest of the roughness elements upwards to the region very close to the roughness crests, while the positive $\tilde{C}_{K,11}$ may be associated with the high-$(\tilde{u})$ speed region that brings a small fraction of $\langle\tilde{u}\tilde{u}\rangle$ from the region very close to the roughness crests downwards towards the wall. The critical difference between the wall-normal turbulent momentum transfer and wall-normal dispersive momentum transfer is that the former can occur between inner and outer regions, such as those for smooth-wall flows, which peaks at the streamwise turbulence intensity profile. On the other hand, wall-normal dispersive momentum transfer, for the present roughness type, only occurs locally at the roughness sublayer (attributed to the local strong mean shear), which peaks at the streamwise dispersive intensity profile, and it can be seen that $\tilde{C}_{K,11}$ approaches zero immediately above $y_e^+ \simeq k_e^+$.

Finally, the intercomponent transfer T_{ij} term for the smooth-wall case is necessarily zero because of the spatial homogeneity and ergodicity, implying that $\widetilde{u_i} \simeq 0$. For the rough-wall case, the intercomponent transfer term T_K for the K' and $\tilde{K}$ transports in (3.7) and (3.8) is given by

$$T_K(x, y) = \frac{1}{2}\langle T_{ii}\rangle = \left\langle \tilde{u}_i \partial_k (\overline{u_i' u_k'}) \right\rangle = \left\langle \tilde{u}_i (\overline{u_k' \partial_k u_i'}) \right\rangle. \tag{3.14}$$

The T_K term in the transport equations provides further insight into how energy is redistributed between K' and $\tilde{K}$ because of its interpretation in (3.7) and (3.8) (see also Appendix A). It is evident that T_K is the product of the dispersive velocity fluctuations and the spatial gradients of the Reynolds stresses. Therefore, this may be interpreted as a term that relates the kinetic energy transfer between K' and $\tilde{K}$ along the streamwise and wall-normal directions to the anisotropic distribution of the Reynolds stresses. The intercomponent transfer T_K of K' and $\tilde{K}$ is shown in figure 10(*d*). The results suggest that energy is mainly transferred from $\tilde{K}$ to K', which is particularly significant only in the near-wall region below $y_e^+ < k_e^+$. This energy transfer mainly results from the product of the streamwise dispersive velocity and the anisotropic distributions of the turbulent momentum fluxes, i.e. $\tilde{u}(\overline{\partial_x u'u'})$, $\tilde{u}(\overline{\partial_y u'v'})$ and $\tilde{u}(\overline{\partial_z u'w'})$ and the spanwise counterparts, as shown in the inset plot of figure 10(*d*) for the case rDNS1. The terms are expressed by considering continuity, i.e. the right-hand side of (3.14). Similar trends are observed for rDNS2 and rDNS3 (not shown for brevity). The dominant contributions to T_K are by the streamwise T_{11} and spanwise T_{33} components. The contribution from the wall-normal component T_{22} is minimal. In addition, only a small positive contribution of T_{22} is found above $y_e^+ \simeq k_e^+$. At the same location, the streamwise T_{11} is negative, which indicates an energy transfer from K' to $\tilde{K}$. It can be concluded that this energy transfer can be attributed to the wall-normal gradient of the Reynolds shear stress $\tilde{u}(\overline{\partial_y u'v'})$ but not due to $\tilde{u}\,(\overline{\partial_x u'u'})$ and $\tilde{u}(\overline{\partial_z u'w'})$.

In this section two energy transports, K' transport and $\tilde{K}$ transport, have been analysed (figures 9 and 10). The K' transport relates to the turbulent flow itself. The $\tilde{K}$ transport relates to the additional stresses induced by the spatial inhomogeneity in the roughness canopy, which is analogous to the K' transport, but mainly resides within the roughness sublayer $(y_e^+ < y_r^+)$ for the present regular roughness type. For the K' transport, the near-wall profiles for the rough-wall cases differ from the smooth-wall case. The energy

redistribution among the spatial transport D'_K, the convection C'_K and intercomponent transfer T_K exhibits qualitatively different behaviours, where the latter two would otherwise be negligible in the smooth-wall case. However, results suggest that the rough wall does not appear to influence the K' transport in the outer region. The K' transport profiles show good collapse to the smooth-wall profiles away from the roughness sublayer. On the other hand, in this study, the $\tilde{K}$ transport was found to be localised to the roughness sublayer. The spatial redistribution of $\tilde{K}$ is among the three terms, namely dispersive convection, dispersive viscous transport and dispersive spatial transport. The local imbalance between production, dissipation, and spatial transport terms is transferred to the K' balance by the T_K term. The T_K term can be interpreted as the local transfer among the K' and $\tilde{K}$ components, as formulated in (3.6) and (3.8). The results show that the leading energy transfer is from $\tilde{K}$ to K' at $y_e^+ \lesssim k_e^+$, which is driven by the spatial gradients of three Reynolds stress components: $\partial_x(\overline{u'u'})$; $\partial_y(\overline{u'v'})$; and $\partial_z(\overline{u'w'})$. There is also a relatively small reverse energy transfer from K' to $\tilde{K}$ occurring just above $y_e^+ \simeq k_e^+$, which is driven by the wall-normal gradient of the Reynolds shear stress $\partial_y(\overline{u'v'})$.

Finally, it must be emphasised that the present findings seem to apply to rough-wall TBLs where the dispersive stress is predominantly localised near the roughness elements. For example, Womack *et al.* (2022) reported differences in the distribution of dispersive stress between regularly and randomly arranged truncated cones, where the dispersive stress was found to be negligible in the case of regular arrangements. Conversely, in the case of the random arrangements, strong secondary flows were observed over the random roughness, leading to significant dispersive stress distributions and a substantial influence on the outer layer. In this study, we have demonstrated that the dispersive stress distributions can be decomposed into various terms associated with the Reynolds stress and dispersive stress transport equations. This methodology may serve as an alternative approach to investigate the significant differences in the individual terms of the transport equations between regularly and irregularly arranged roughness elements, which govern the generation and transport of TKE, Reynolds shear stress, and dispersive stresses. It also enables the examination of the transfer between turbulent and dispersive stress tensors. Understanding the generation mechanisms of secondary flows above the roughness may be a crucial step towards better comprehending the outer-layer similarity.

4. Conclusions

The DNS of a spatially developing ZPG TBL with three-dimensional sinusoidal roughness was carried out at approximately the momentum thickness Reynolds number range $Re_\theta = 4820$–7530, corresponding to $Re_\tau = 1780$–2820. The roughness elements are generated by a product of cosine functions, modelled by the IBM.

Comparisons were made with a DNS of smooth-wall TBL at a similar friction Reynolds number. Estimations of the Hama roughness function ΔU^+ confirmed that all cases are within the fully rough regime. This study reported the equivalent sand grain roughness, relevant roughness length scales and global boundary layer parameters. Analyses of the sinusoidal roughness effects were performed using the double-averaging procedure to decompose the velocity fluctuations into turbulent and dispersive components. The dispersive component is associated with the spatial inhomogeneity induced by the varying surface elevations. Mean and second-order rough-wall flow statistics show collapse to the smooth-wall flow statistics, suggesting that the roughness effects are likely to be confined within the roughness sublayer for this particular roughness. The results support that the wall-similarity may still hold between the present smooth-wall and rough-wall TBLs with

three-dimensional sinusoidal roughness. This finding is consistent with the conclusions of numerical studies of pipe and channel flows with three-dimensional sinusoidal roughness in the literature. The sinusoidal roughness effect is further investigated by the triple-decomposed transport equations of the total, Reynolds and dispersive stress tensors, using a formulation that is analogous to the classic Reynolds stress transport equation (Appendix A). In addition to the classic transport equation of the TKE ($K' = (1/2)\langle\overline{u_i'^2}\rangle$) that characterises the energy balance in a TBL, an additional transport equation that quantifies the dispersive kinetic energy ($\tilde{K} = (1/2)\langle\tilde{u}_i^2\rangle$) balance has also been investigated in detail. The results show that the K' transport of the rough-wall TBL is substantially different from those of the smooth-wall TBL due to the production by the mean shear, which is strongest at the roughness crests. Results also show that the spatial redistribution of $\tilde{K}$ is among the spatial transport (D'_K), the convection (C'_K) and the intercomponent transfer (T_K). In particular, the spatial transport of K' is greatly influenced by two additional turbulent-dispersive spatial fluxes arising due to the roughness-induced dispersive velocity fluctuations, namely $(\overline{u_i'u_i'}\tilde{u}_k)$ and $(\overline{u_i'u_k'}\tilde{u}_i)$. The convection of K' can be approximated by the mean streamwise flow. In addition, the wall-normal secondary flow played a critical role in redistributing the wall-parallel turbulent momentum fluxes. The intercomponent energy transfer between K' and $\tilde{K}$ (i.e. T_K) was further analysed. The T_K is mainly driven by the local anisotropic distribution of the Reynolds stress components associated with the streamwise dispersive fluctuation: $\tilde{u}\partial_x(\overline{u'u'})$; $\tilde{u}\partial_y(\overline{u'v'})$; and $\tilde{u}\partial_z(\overline{u'w'})$ and the spanwise counterparts. Overall, the profiles of the K' transport show good collapse to the smooth-wall profiles only in the outer region, resembling a smooth-wall TBL, providing evidence for the wall similarity hypothesis (figures 9 and 10). In contrast to the K' transport, the analysis of the $\tilde{K}$ transport revealed that the $\tilde{K}$ transport is likely a local phenomenon for the present roughness type, presumably due to the primary mean shear found in the vicinity of the roughness crests within the roughness sublayer. It was observed that the primary mean shear plays a crucial role in the $\tilde{K}$ transport, leading to enhanced dispersive momentum flux localised to the roughness crests.

Funding. The authors acknowledge the financial support of the Australian Research Council. This work was supported with supercomputing resources provided by the Phoenix HPC service at the University of Adelaide. This research was also undertaken with the assistance of resources provided at the NCI NF through the Computational Merit Allocation Scheme, supported by the Australian Government and the Pawsey Supercomputing Centre, with funding from the Australian Government and the Government of Western Australia.

Declaration of interests. The authors report no conflict of interest.

Author ORCIDs.
C.I. Chan https://orcid.org/0000-0002-0707-6265;
R.C. Chin https://orcid.org/0000-0002-2709-4321.

Appendix A. Stresses balance between total, Reynolds and dispersive components

The governing equation for incompressible fluid with constant density and viscosity is the incompressible Navier–Stokes equations, assuming zero forcing (e.g. zero gravity), it is given by

$$\partial_t(u_i) + (u_k)\partial_k(u_i) = -\frac{1}{\rho}\partial_i(p) + \nu\Delta(u_i), \tag{A1}$$

$$\partial_i u_i = 0, \tag{A2}$$

where $\partial_t \equiv \partial()/\partial t$, $\partial_i \equiv \partial()/\partial x_i$ and $\Delta \equiv \partial_k^2$. The streamwise, wall-normal and spanwise coordinates are denoted as x_i $(i = 1, 2, 3)$ or $\boldsymbol{x} = (x, y, z)$, interchangeably. The corresponding instantaneous velocity components are denoted as u_i or $\boldsymbol{u} = (u, v, w)$, interchangeably, and p is the pressure. The flow velocity and pressure are decomposed into mean and total fluctuation components based on (2.6). The total velocity (and pressure) fluctuation can be further decomposed into a turbulent component and a dispersive component written as (Raupach *et al.* 1991)

$$u_i(\boldsymbol{x}, t) = U_i(x, y) + \underbrace{u_i''(\boldsymbol{x}, t)}_{total} = U_i(x, y) + \underbrace{u_i'(\boldsymbol{x}, t)}_{turbulent} + \underbrace{\tilde{u}_i(\boldsymbol{x})}_{dispersive}, \tag{A3}$$

and

$$\partial_i U_i = 0, \quad \partial_i u_i' = 0, \quad \partial_i \tilde{u}_i = 0. \tag{A4}$$

Substituting (A3) into (A1). We then multiply the governing equation by u_j'' and take the temporal average of the resulting equation, assuming the Reynolds conditions (Monin & Yaglom 1975). By interchanging the i and j and adding up the resulting equations, we obtain

$$\begin{aligned}
&\partial_t(\overline{u_i'' u_j''}) + \tilde{u}_i U_k \partial_k U_j + \tilde{u}_j U_k \partial_k U_i + U_k \partial_k(\overline{u_i'' u_j''}) \\
&\quad = -\overline{u_i'' u_k''}\partial_k U_j - \overline{u_j'' u_k''}\partial_k U_i - \partial_k(\overline{u_i'' u_j'' u_k''}) \\
&\qquad - \frac{1}{\rho}\left[\tilde{u}_j \partial_i P + \tilde{u}_i \partial_j P + \overline{u_i'' \partial_j p''} + \overline{u_j'' \partial_i p''}\right] \\
&\qquad + \nu \tilde{u}_i \Delta U_j + \nu \tilde{u}_j \Delta U_i + \nu \Delta(\overline{u_i'' u_j''}) - 2\nu \overline{\partial_k u_i'' \partial_k u_j''},
\end{aligned} \tag{A5}$$

where the transport equation for the total stress tensor is obtained: $C_{ij}''(\boldsymbol{x}) := \tilde{u}_i U_k \partial_k U_j + \tilde{u}_j U_k \partial_k U_i + U_k \partial_k(\overline{u_i'' u_j''})$ is the total convection; $P_{ij}''(\boldsymbol{x}) := -\overline{u_i'' u_k''}\partial_k U_j - \overline{u_j'' u_k''}\partial_k U_i$ is the total production; $D_{ij}''(\boldsymbol{x}) := -\partial_k(\overline{u_i'' u_j'' u_k''})$ is the total spatial transport; $\Pi_{ij}''(\boldsymbol{x}) := -(1/\rho)[\tilde{u}_j \partial_i P + \tilde{u}_i \partial_j P + \overline{u_i'' \partial_j p''} + \overline{u_j'' \partial_i p''}]$ is the total pressure transport; $D_{\nu,ij}''(\boldsymbol{x}) := \nu \tilde{u}_i \Delta U_j + \nu \tilde{u}_j \Delta U_i + \nu \Delta(\overline{u_i'' u_j''})$ is the total viscous transport; $\epsilon_{ij}''(\boldsymbol{x}) := 2\nu \overline{\partial_k u_i'' \partial_k u_j''}$ is the total viscous dissipation, cf. (3.6). The term $\partial_k(\overline{u_i'' u_j'' u_k''})$ can be decomposed as follows:

$$\partial_k(\overline{u_i'' u_j'' u_k''}) = \partial_k(\overline{u_i' u_j' u_k'}) + \partial_k(\tilde{u}_k \overline{u_i' u_j'}) + \partial_k(\tilde{u}_j \overline{u_i' u_k'}) + \partial_k(\tilde{u}_i \overline{u_j' u_k'}) + \partial_k(\tilde{u}_i \tilde{u}_j \tilde{u}_k), \tag{A6}$$

by the product rule, (A3) and (A4). Clearly, this decomposition is not unique, but is chosen to show later that the first four terms on the right-hand side of (A6) are the turbulent and turbulent-dispersive spatial transport terms in (A10) and the last term is the dispersive spatial transport term in (A11). Obtaining the transport equation for the Reynolds stress tensor is similar. We first substitute (A3) into (A1). We then multiply the resulting equation by u_j' and take the temporal-average of the resulting equation. By interchanging the i and j and adding up the resulting equation, we obtain

$$\begin{aligned}
\partial_t(\overline{u_i' u_j'}) + U_k \partial_k(\overline{u_i' u_j'}) &= -\overline{u_i' u_k'}\partial_k U_j - \overline{u_j' u_k'}\partial_k U_i - \partial_k(\overline{u_i' u_j' u_k'}) \\
&\quad - \tilde{u}_k \partial_k(\overline{u_i' u_j'}) - \overline{u_i' u_k'}\partial_k \tilde{u}_j - \overline{u_j' u_k'}\partial_k \tilde{u}_i \\
&\quad - \frac{1}{\rho}\left[\overline{u_i' \partial_j p'} + \overline{u_j' \partial_i p'}\right] + \nu \Delta(\overline{u_i' u_j'}) - 2\nu \overline{\partial_k u_i' \partial_k u_j'}.
\end{aligned} \tag{A7}$$

By the product rule and (A4), we have the following terms written as:

$$\tilde{u}_k \partial_k(\overline{u_i' u_j'}) = \partial_k(\overline{u_i' u_j'} \tilde{u}_k), \tag{A8}$$

$$\overline{u_i' u_k'} \partial_k \tilde{u}_j + \overline{u_j' u_k'} \partial_k \tilde{u}_i = \partial_k(\overline{u_i' u_k'} \tilde{u}_j) + \partial_k(\overline{u_j' u_k'} \tilde{u}_i) - \tilde{u}_i(\overline{u_k' \partial_k u_j'}) - \tilde{u}_j(\overline{u_k' \partial_k u_i'}), \tag{A9}$$

and (A7) can be written as

$$\begin{aligned} \partial_t(\overline{u_i' u_j'}) + U_k \partial_k(\overline{u_i' u_j'}) = & -\overline{u_i' u_k'} \partial_k U_j - \overline{u_j' u_k'} \partial_k U_i - \partial_k(\overline{u_i' u_j' u_k'}) \\ & - \partial_k(\overline{u_i' u_j'} \tilde{u}_k) - \partial_k(\overline{u_i' u_k'} \tilde{u}_j) - \partial_k(\overline{u_j' u_k'} \tilde{u}_i) + \tilde{u}_i(\overline{u_k' \partial_k u_j'}) + \tilde{u}_j(\overline{u_k' \partial_k u_i'}) \\ & - \frac{1}{\rho}\left[\overline{u_i' \partial_j p'} + \overline{u_j' \partial_i p'}\right] + \nu \Delta(\overline{u_i' u_j'}) - 2\nu \overline{\partial_k u_i' \partial_k u_j'}, \end{aligned} \tag{A10}$$

where $C_{ij}'(\boldsymbol{x}) := U_k \partial_k(\overline{u_i' u_j'})$ is the turbulent convection; $P_{ij}'(\boldsymbol{x}) := -\overline{u_i' u_k'} \partial_k U_j - \overline{u_j' u_k'} \partial_k U_i$ is the turbulent production; $D_{ij}'(\boldsymbol{x}) := -\partial_k(\overline{u_i' u_j' u_k'}) - \partial_k(\overline{u_i' u_j'} \tilde{u}_k) - \partial_k(\overline{u_i' u_k'} \tilde{u}_j) - \partial_k(\overline{u_j' u_k'} \tilde{u}_i)$ is the turbulent spatial transport; $T_{ij}(\boldsymbol{x}) := \tilde{u}_i(\overline{u_k' \partial_k u_j'}) + \tilde{u}_j(\overline{u_k' \partial_k u_i'})$ is the intercomponent transfer; $\Pi_{ij}'(\boldsymbol{x}) := -(1/\rho)[\overline{u_i' \partial_j p'} + \overline{u_j' \partial_i p'}]$ is the turbulent pressure transport; $D_{\nu,ij}'(\boldsymbol{x}) := \nu \Delta(\overline{u_i' u_j'})$ is the turbulent viscous transport; $\epsilon_{ij}'(\boldsymbol{x}) := 2\nu \overline{\partial_k u_i' \partial_k u_j'}$ is the turbulent viscous dissipation, cf. (3.7). When $\tilde{u}_i = 0$, (A10) is the Reynolds stress transport equation (Rotta 1951; Tennekes & Lumley 1972; Pope 2000) and each term is equivalent to the corresponding term in (A5), except that the intercomponent transfer is $T_{ij} = 0$. To obtain the transport equation for dispersive momentum flux, we multiply (A1) by $\tilde{u}_j$ and take the temporal average of the resulting equation. By interchanging the i and j and adding up the resulting equation, we obtain

$$\begin{aligned} & \tilde{u}_i U_k \partial_k U_j + \tilde{u}_j U_k \partial_k U_i + U_k \partial_k(\tilde{u}_i \tilde{u}_j) \\ & \quad = -\tilde{u}_i \tilde{u}_k \partial_k U_j - \tilde{u}_j \tilde{u}_k \partial_k U_i - \partial_k(\tilde{u}_i \tilde{u}_j \tilde{u}_k) - \tilde{u}_i(\overline{u_k' \partial_k u_j'}) - \tilde{u}_j(\overline{u_k' \partial_k u_i'}) \\ & \qquad - \frac{1}{\rho}\left[\tilde{u}_j \partial_i P + \tilde{u}_i \partial_j P + \tilde{u}_i \partial_j \tilde{p} + \tilde{u}_j \partial_i \tilde{p}\right] + \nu \tilde{u}_i \Delta U_j + \nu \tilde{u}_j \Delta U_i + \nu \Delta \tilde{u}_i \tilde{u}_j - 2\nu \partial_k \tilde{u}_i \partial_k \tilde{u}_j, \end{aligned} \tag{A11}$$

where $\tilde{C}_{ij}(\boldsymbol{x}) := \tilde{u}_i U_k \partial_k U_j + \tilde{u}_j U_k \partial_k U_i + U_k \partial_k(\tilde{u}_i \tilde{u}_j)$ is the dispersive convection; $\tilde{P}_{ij}(\boldsymbol{x}) := -\tilde{u}_i \tilde{u}_k \partial_k U_j - \tilde{u}_j \tilde{u}_k \partial_k U_i$ is the dispersive production; $\tilde{D}_{ij}(\boldsymbol{x}) := -\partial_k(\tilde{u}_i \tilde{u}_j \tilde{u}_k)$ is the dispersive spatial transport; where $-T_{ij}(\boldsymbol{x}) := -\tilde{u}_i(\overline{u_k' \partial_k u_j'}) - \tilde{u}_j(\overline{u_k' \partial_k u_i'})$ is the intercomponent transfer as shown in (A10) with opposite signs; $\tilde{\Pi}_{ij}(\boldsymbol{x}) := -(1/\rho)[\tilde{u}_j \partial_i P + \tilde{u}_i \partial_j P + \tilde{u}_i \partial_j \tilde{p} + \tilde{u}_j \partial_i \tilde{p}]$ is the dispersive pressure transport; $\tilde{D}_{\nu,ij}(\boldsymbol{x}) := \nu \tilde{u}_i \Delta U_j + \nu \tilde{u}_j \Delta U_i + \nu \Delta \tilde{u}_i \tilde{u}_j$ is the dispersive viscous transport; $\tilde{\epsilon}_{ij}(\boldsymbol{x}) := 2\nu \partial_k \tilde{u}_i \partial_k \tilde{u}_j$ is the dispersive viscous dissipation, cf. (3.8). By combining the two equations (A10) and (A11) together, we obtain (A5) as the term T_{ij} cancels out, and combining D_{ij}' in (A10) and $\tilde{D}_{ij}$ in (A11), we obtain D_{ij}'' by using (A6). The other terms can be reconstructed in a similar fashion according to (2.9).

References

Abdelaziz, M., Djenidi, L., Ghayesh, M.H. & Chin, R. 2022 A new equivalent sand grain roughness relation for two-dimensional rough wall turbulent boundary layers. *J. Fluid Mech.* **940**, A25.

Alfredsson, P.H., Örlü, R. & Segalini, A. 2012 A new formulation for the streamwise turbulence intensity distribution in wall-bounded turbulent flows. *Eur. J. Mech. (B/Fluids)* **36**, 167–175.

ALFREDSSON, P.H., SEGALINI, A. & ÖRLÜ, R. 2011 A new scaling for the streamwise turbulence intensity in wall-bounded turbulent flows and what it tells us about the 'outer' peak. *Phys. Fluids* **23** (4), 041702.

ALFREDSSON, P.H., SEGALINI, A. & ÖRLÜ, R. 2021 The diagnostic plot – a tutorial with a ten year perspective. In *Progress in Turbulence IX* (ed. R. Örlü, A. Talamelli, J. Peinke & M. Oberlack), pp. 125–135. Springer.

AMIR, M. & CASTRO, I.P. 2011 Turbulence in rough-wall boundary layers: universality issues. *Exp. Fluids* **51** (2), 313–326.

ANDERSON, W., BARROS, J.M., CHRISTENSEN, K.T. & AWASTHI, A. 2015 Numerical and experimental study of mechanisms responsible for turbulent secondary flows in boundary layer flows over spanwise heterogeneous roughness. *J. Fluid Mech.* **768**, 316–347.

BAILEY, S.C.C. & SMITS, A.J. 2010 Experimental investigation of the structure of large- and very-large-scale motions in turbulent pipe flow. *J. Fluid Mech.* **651**, 339–356.

BAILEY, B.N. & STOLL, R. 2013 Turbulence in sparse, organized vegetative canopies: a large-eddy simulation study. *Boundary-Layer Meteorol.* **147** (3), 369–400.

BENDAT, J.S. & PIERSOL, A.G. 2011 *Random Data: Analysis and Measurement Procedures*, vol. 729. John Wiley & Sons.

BLACKMAN, K. & PERRET, L. 2016 Non-linear interactions in a boundary layer developing over an array of cubes using stochastic estimation. *Phys. Fluids* **28** (9), 095108.

BRZEK, B., CAL, R.B., JOHANSSON, G. & CASTILLO, L. 2007 Inner and outer scalings in rough surface zero pressure gradient turbulent boundary layers. *Phys. Fluids* **19** (6), 065101.

BRZEK, B.G., CAL, R.B., JOHANSSON, G. & CASTILLO, L. 2008 Transitionally rough zero pressure gradient turbulent boundary layers. *Exp. Fluids* **44**, 115–124.

BUSSE, A., LÜTZNER, M. & SANDHAM, N.D. 2015 Direct numerical simulation of turbulent flow over a rough surface based on a surface scan. *Comput. Fluids* **116**, 129–147.

BUSSE, A., THAKKAR, M. & SANDHAM, N.D. 2017 Reynolds-number dependence of the near-wall flow over irregular rough surfaces. *J. Fluid Mech.* **810**, 196–224.

CARDILLO, J., CHEN, Y., ARAYA, G., NEWMAN, J., JANSEN, K. & CASTILLO, L. 2013 DNS of a turbulent boundary layer with surface roughness. *J. Fluid Mech.* **729**, 603–637.

CASTRO, I.P., CHENG, H. & REYNOLDS, R. 2006 Turbulence over urban-type roughness: deductions from wind-tunnel measurements. *Boundary-Layer Meteorol.* **118** (1), 109–131.

CASTRO, I.P., SEGALINI, A. & ALFREDSSON, P.H. 2013 Outer-layer turbulence intensities in smooth- and rough-wall boundary layers. *J. Fluid Mech.* **727**, 119–131.

CHAN, C.I., ÖRLÜ, R., SCHLATTER, P. & CHIN, R.C. 2022 Large-scale and small-scale contribution to the skin friction reduction in a modified turbulent boundary layer by a large-eddy break-up device. *Phys. Rev. Fluids* **7**, 034601.

CHAN, C.I. & CHIN, R.C. 2022 Investigation of the influence of miniature vortex generators on the large-scale motions of a turbulent boundary layer. *J. Fluid Mech.* **932**, A29.

CHAN, L., MACDONALD, M., CHUNG, D., HUTCHINS, N. & OOI, A. 2015 A systematic investigation of roughness height and wavelength in turbulent pipe flow in the transitionally rough regime. *J. Fluid Mech.* **771**, 743–777.

CHAN, L., MACDONALD, M., CHUNG, D., HUTCHINS, N. & OOI, A. 2018 Secondary motion in turbulent pipe flow with three-dimensional roughness. *J. Fluid Mech.* **854**, 5–33.

CHAN, C.I., SCHLATTER, P. & CHIN, R.C. 2021 Interscale transport mechanisms in turbulent boundary layers. *J. Fluid Mech.* **921**, A13.

CHAN-BRAUN, C., GARCÍA-VILLALBA, M. & UHLMANN, M. 2011 Force and torque acting on particles in a transitionally rough open-channel flow. *J. Fluid Mech.* **684**, 441–474.

CHENG, C., SHYY, W. & FU, L. 2022 Streamwise inclination angle of wall-attached eddies in turbulent channel flows. *J. Fluid Mech.* **946**, A49.

CHEVALIER, M., LUNDBLADH, A. & HENNINGSON, D.S. 2007 Simson – a pseudo-spectral solver for incompressible boundary layer flow. *Tech. Rep. TRITA-MEK 2007:07*. KTH Mechanics.

CHOI, H. & MOIN, P. 1994 Effects of the computational time step on numerical solutions of turbulent flow. *J. Comput. Phys.* **113** (1), 1–4.

CHUNG, D., HUTCHINS, N., SCHULTZ, M.P. & FLACK, K.A. 2021 Predicting the drag of rough surfaces. *Annu. Rev. Fluid Mech.* **53** (1), 439–471.

COCEAL, O., DOBRE, A., THOMAS, T.G. & BELCHER, S.E. 2007*a* Structure of turbulent flow over regular arrays of cubical roughness. *J. Fluid Mech.* **589**, 375–409.

COCEAL, O., THOMAS, T.G. & BELCHER, S.E. 2007*b* Spatial variability of flow statistics within regular building arrays. *Boundary-Layer Meteorol.* **125** (3), 537–552.

COCEAL, O., THOMAS, T.G., CASTRO, I.P. & BELCHER, S.E. 2006 Mean flow and turbulence statistics over groups of urban-like cubical obstacles. *Boundary-Layer Meteorol.* **121**, 491–519.

DESHPANDE, R., MONTY, J.P. & MARUSIC, I. 2019 Streamwise inclination angle of large wall-attached structures in turbulent boundary layers. *J. Fluid Mech.* **877**, R4.

FLACK, K.A. & SCHULTZ, M.P. 2010 Review of hydraulic roughness scales in the fully rough regime. *Trans. ASME J. Fluids Engng* **132**, 0412031.

FLACK, K.A. & SCHULTZ, M.P. 2014 Roughness effects on wall-bounded turbulent flows. *Phys. Fluids* **26** (10), 101305.

FLACK, K.A., SCHULTZ, M.P. & CONNELLY, J.S. 2007 Examination of a critical roughness height for outer layer similarity. *Phys. Fluids* **19** (9), 095104.

FLACK, K.A., SCHULTZ, M.P. & SHAPIRO, T.A. 2005 Experimental support for Townsend's Reynolds number similarity hypothesis on rough walls. *Phys. Fluids* **17** (3), 035102.

FOROOGHI, P., STROH, A., MAGAGNATO, F., JAKIRLIĆ, S. & FROHNAPFEL, B. 2017 Toward a universal roughness correlation. *Trans. ASME J. Fluids Engng* **139** (12), 121201.

FOROOGHI, P., STROH, A., SCHLATTER, P. & FROHNAPFEL, B. 2018 Direct numerical simulation of flow over dissimilar, randomly distributed roughness elements: a systematic study on the effect of surface morphology on turbulence. *Phys. Rev. Fluids* **3** (4), 044605.

GANJU, S., BAILEY, S.C.C. & BREHM, C. 2022 Amplitude and wavelength scaling of sinusoidal roughness effects in turbulent channel flow at fixed $Re_\tau = 720$. *J. Fluid Mech.* **937**, A22.

GUALA, M., HOMMEMA, S.E. & ADRIAN, R.J. 2006 Large-scale and very-large-scale motions in turbulent pipe flow. *J. Fluid Mech.* **554**, 521–542.

HAMA, F.R. 1954 Boundary layer characteristics for smooth and rough surfaces. *Trans. Soc. Nav. Archit. Mar. Engrs* **62**, 333–358.

HUTCHINS, N. & MARUSIC, I. 2007 Evidence of very long meandering features in the logarithmic region of turbulent boundary layers. *J. Fluid Mech.* **579**, 1–28.

HWANG, H.G. & LEE, J.H. 2018 Secondary flows in turbulent boundary layers over longitudinal surface roughness. *Phys. Rev. Fluids* **3**, 014608.

JIMÉNEZ, J. 2004 Turbulent flows over rough walls. *Annu. Rev. Fluid Mech.* **36** (1), 173–196.

KADIVAR, M., TORMEY, D. & MCGRANAGHAN, G. 2021 A review on turbulent flow over rough surfaces: fundamentals and theories. *Intl J. Thermofluids* **10**, 100077.

KIM, K.C. & ADRIAN, R.J. 1999 Very large-scale motion in the outer layer. *Phys. Fluids* **11** (2), 417–422.

KROGSTAD, P.-Å., ANDERSSON, H.I., BAKKEN, O.M. & ASHRAFIAN, A. 2005 An experimental and numerical study of channel flow with rough walls. *J. Fluid Mech.* **530**, 327–352.

KROGSTAD, P.-Å. & ANTONIA, R.A. 1994 Structure of turbulent boundary layers on smooth and rough walls. *J. Fluid Mech.* **277**, 1–21.

KROGSTAD, P.-Å. & ANTONIA, R.A. 1999 Surface roughness effects in turbulent boundary layers. *Exp. Fluids* **27** (5), 450–460.

KROGSTAD, P.-Å., ANTONIA, R.A. & BROWNE, L.W.B. 1992 Comparison between rough- and smooth-wall turbulent boundary layers. *J. Fluid Mech.* **245**, 599–617.

KROGSTAD, P.-Å. & EFROS, V. 2012 About turbulence statistics in the outer part of a boundary layer developing over two-dimensional surface roughness. *Phys. Fluids* **24** (7), 075112.

KUMAR, P. & MAHESH, K. 2021 Simple model for mean stress in turbulent boundary layers. *Phys. Rev. Fluids* **6**, 024603.

KUMAR, P. & MAHESH, K. 2022 A method to determine wall shear stress from mean profiles in turbulent boundary layers. *Exp. Fluids* **63** (1), 1–18.

LEE, J.H., SEENA, A., LEE, S.-H. & SUNG, H.J. 2012 Turbulent boundary layers over rod- and cube-roughened walls. *J. Turbul.* **13**, N40.

LEE, S.-H. & SUNG, H.J. 2007 Direct numerical simulation of the turbulent boundary layer over a rod-roughened wall. *J. Fluid Mech.* **584**, 125–146.

LEE, J.H., SUNG, H.J. & KROGSTAD, P.Å. 2011 Direct numerical simulation of the turbulent boundary layer over a cube-roughened wall. *J. Fluid Mech.* **669**, 397–431.

LEONARDI, S. & CASTRO, I.P. 2010 Channel flow over large cube roughness: a direct numerical simulation study. *J. Fluid Mech.* **651**, 519–539.

MA, R., ALAMÉ, K. & MAHESH, K. 2021 Direct numerical simulation of turbulent channel flow over random rough surfaces. *J. Fluid Mech.* **908**, A40.

MA, G.Z., XU, C.X., SUNG, H.J. & HUANG, W.X. 2020 Scaling of rough-wall turbulence by the roughness height and steepness. *J. Fluid Mech.* **900**, R7.

MACDONALD, M., CHAN, L., CHUNG, D., HUTCHINS, N. & OOI, A. 2016 Turbulent flow over transitionally rough surfaces with varying roughness densities. *J. Fluid Mech.* **804**, 130–161.

MARUSIC, I. & HEUER, W.D.C. 2007 Reynolds number invariance of the structure inclination angle in wall turbulence. *Phys. Rev. Lett.* **99**, 114504.

MARUSIC, I., MONTY, J.P., HULTMARK, M. & SMITS, A.J. 2013 On the logarithmic region in wall turbulence. *J. Fluid Mech.* **716**, R3.

MEDJNOUN, T., RODRIGUEZ-LOPEZ, E., FERREIRA, M.A., GRIFFITHS, T., MEYERS, J. & GANAPATHISUBRAMANI, B. 2021 Turbulent boundary-layer flow over regular multiscale roughness. *J. Fluid Mech.* **917**, A1.

MOIN, P. & MAHESH, K. 1998 Direct numerical simulation: a tool in turbulence research. *Annu. Rev. Fluid Mech.* **30** (1), 539–578.

MONIN, A.S. & YAGLOM, A.M. 1975 *Statistical Fluid Mechanics: Mechanics of Turbulence*. MIT Press.

MONTY, J.P., ALLEN, J.J., LIEN, K. & CHONG, M.S. 2011 Modification of the large-scale features of high Reynolds number wall turbulence by passive surface obtrusions. *Exp. Fluids* **51** (6), 1755–1763.

MONTY, J.P., HUTCHINS, N., NG, H.C.H., MARUSIC, I. & CHONG, M.S. 2009 A comparison of turbulent pipe, channel and boundary layer flows. *J. Fluid Mech.* **632**, 431–442.

NADEEM, M., LEE, J.H., LEE, J. & SUNG, H.J. 2015 Turbulent boundary layers over sparsely-spaced rod-roughened walls. *Intl J. Heat Fluid Flow* **56**, 16–27.

NAPOLI, E., ARMENIO, V. & DE-MARCHIS, M. 2008 The effect of the slope of irregularly distributed roughness elements on turbulent wall-bounded flows. *J. Fluid Mech.* **613**, 385–394.

NIKORA, V., GORING, D., MCEWAN, I. & GRIFFITHS, G. 2001 Spatially averaged open-channel flow over rough bed. *ASCE J. Hydraul. Engng* **127** (2), 123–133.

NIKURADSE, J. 1933 Strömungsgesetze in rauhen Rohren. *VDI-Forsch.* **361**.

NUGROHO, B., HUTCHINS, N. & MONTY, J.P. 2013 Large-scale spanwise periodicity in a turbulent boundary layer induced by highly ordered and directional surface roughness. *Intl J. Heat Fluid Flow* **41**, 90–102.

PERRY, A.E. & LI, J.D. 1990 Experimental support for the attached-eddy hypothesis in zero-pressure-gradient turbulent boundary layers. *J. Fluid Mech.* **218**, 405–438.

PLACIDI, M. & GANAPATHISUBRAMANI, B. 2018 Turbulent flow over large roughness elements: effect of frontal and plan solidity on turbulence statistics and structure. *Boundary-Layer Meteorol.* **167** (1), 99–121.

POGGI, D., KATUL, G.G. & ALBERTSON, J.D. 2004 A note on the contribution of dispersive fluxes to momentum transfer within canopies. *Boundary-Layer Meteorol.* **111** (3), 615–621.

POPE, S.B. 2000 *Turbulent Flows*. Cambridge University Press.

RAUPACH, M.R., ANTONIA, R.A. & RAJAGOPALAN, S. 1991 Rough-wall turbulent boundary layers. *Appl. Mech. Rev.* **44** (1), 1–25.

RAUPACH, M.R. & SHAW, R.H. 1982 Averaging procedures for flow within vegetation canopies. *Boundary-Layer Meteorol.* **22**, 79–90.

ROTTA, J. 1951 Statistische theorie nichthomogener turbulenz. *Z. Phys.* **129** (6), 547–572.

SCHLATTER, P. & ÖRLÜ, R. 2010 Assessment of direct numerical simulation data of turbulent boundary layers. *J. Fluid Mech.* **659**, 116–126.

SCHLATTER, P. & ÖRLÜ, R. 2012 Turbulent boundary layers at moderate Reynolds numbers: inflow length and tripping effects. *J. Fluid Mech.* **710**, 5–34.

SCHULTZ, M.P. & FLACK, K.A. 2005 Outer layer similarity in fully rough turbulent boundary layers. *Exp. Fluids* **38** (3), 328–340.

STROH, A., SCHÄFER, K., FROHNAPFEL, B. & FOROOGHI, P. 2020 Rearrangement of secondary flow over spanwise heterogeneous roughness. *J. Fluid Mech.* **885**, R5.

TÜRK, S., DASCHIEL, G., STROH, A., HASEGAWA, Y. & FROHNAPFEL, B. 2014 Turbulent flow over superhydrophobic surfaces with streamwise grooves. *J. Fluid Mech.* **747**, 186–217.

TENNEKES, H. & LUMLEY, J.L. 1972 *A First Course in Turbulence*. MIT Press.

TOMKINS, C.D. & ADRIAN, R.J. 2005 Energetic spanwise modes in the logarithmic layer of a turbulent boundary layer. *J. Fluid Mech.* **545**, 141–162.

TOWNSEND, A.A. 1956 *The Structure of Turbulent Shear Flow*. Cambridge University Press.

VANDERWEL, C., STROH, A., KRIEGSEIS, J., FROHNAPFEL, B. & GANAPATHISUBRAMANI, B. 2019 The instantaneous structure of secondary flows in turbulent boundary layers. *J. Fluid Mech.* **862**, 845–870.

VOLINO, R.J. & SCHULTZ, M.P. 2018 Determination of wall shear stress from mean velocity and Reynolds shear stress profiles. *Phys. Rev. Fluids* **3**, 034606.

VOLINO, R.J., SCHULTZ, M.P. & FLACK, K.A. 2007 Turbulence structure in rough- and smooth-wall boundary layers. *J. Fluid Mech.* **592**, 263–293.

VOLINO, R.J., SCHULTZ, M.P. & FLACK, K.A. 2009 Turbulence structure in a boundary layer with two-dimensional roughness. *J. Fluid Mech.* **635**, 75–101.

VOLINO, R.J., SCHULTZ, M.P. & FLACK, K.A. 2011 Turbulence structure in boundary layers over periodic two- and three-dimensional roughness. *J. Fluid Mech.* **676**, 172–190.

WANGSAWIJAYA, D.D. & HUTCHINS, N. 2022 Investigation of unsteady secondary flows and large-scale turbulence in heterogeneous turbulent boundary layers. *J. Fluid Mech.* **934**, A40.

WOMACK, K.M., MENEVEAU, C. & SCHULTZ, M.P. 2019 Comprehensive shear stress analysis of turbulent boundary layer profiles. *J. Fluid Mech.* **879**, 360–389.

WOMACK, K.M., VOLINO, R.J., MENEVEAU, C. & SCHULTZ, M.P. 2022 Turbulent boundary layer flow over regularly and irregularly arranged truncated cone surfaces. *J. Fluid Mech.* **933**, A38.

WU, Y. & CHRISTENSEN, K.T. 2010 Spatial structure of a turbulent boundary layer with irregular surface roughness. *J. Fluid Mech.* **655**, 380–418.

XU, H.H.A., ALTLAND, S.J., YANG, X.I.A. & KUNZ, R.F. 2021 Flow over closely packed cubical roughness. *J. Fluid Mech.* **920**, A37.

YANG, J. & ANDERSON, W. 2018 Numerical study of turbulent channel flow over surfaces with variable spanwise heterogeneities: topographically-driven secondary flows affect outer-layer similarity of turbulent length scales. *Flow Turbul. Combust.* **100** (1), 1–17.

YANG, X.I.A., SADIQUE, J., MITTAL, R. & MENEVEAU, C. 2016 Exponential roughness layer and analytical model for turbulent boundary layer flow over rectangular-prism roughness elements. *J. Fluid Mech.* **789**, 127–165.

YANG, X.I.A., XU, H.H.A., HUANG, X.L.D. & GE, M.-W. 2019 Drag forces on sparsely packed cube arrays. *J. Fluid Mech.* **880**, 992–1019.

YUAN, J. & PIOMELLI, U. 2014 Numerical simulations of sink-flow boundary layers over rough surfaces. *Phys. Fluids* **26** (1), 015113.